MEASUREMENTS OF SECONDARY MASS FLUX FROM A SURFACE BOMBARDED BY AN [EMIM][BF_4] ELECTROSPRAY PLUME

BY

AVINASH RAO

THESIS

Submitted in partial fulfillment of the requirements
for the degree of Master of Science in Aerospace Engineering
in the Graduate College of the
University of Illinois Urbana-Champaign, 2023

Urbana, Illinois

Adviser:

Professor Joshua L. Rovey

Abstract

Electrospray propulsion systems operate by electrostatically extracting high speed droplets, clusters, and molecules from an ionic liquid propellant. These high speed species can impact and interact with surfaces in proximity of the propulsion device, producing an amorphous plume of secondary species. The aim of this research is to demonstrate a methodology for measuring the mass of a differential component of the secondary plume to better understand how electrospray thrusters interact with their terrestrial test facilities and their in-space environment. Experiments conducted utilized a quartz crystal microbalance to investigate the energy dependence of secondary mass flux as well as the angular distribution of secondary mass for high voltage and low voltage primary electrospray plumes. The secondary mass flux yields was observed to have very little dependence on the energy of the primary plume, with yield values contained within 6.822×10^{-14} $\frac{\text{ng}}{\text{ion-sr}}$ and 8.873×10^{-14} $\frac{\text{ng}}{\text{ion-sr}}$ over an order of magnitude of primary voltages. The angular distribution of the secondary plume produced by a low energy primary plume was relatively flat, with yields ranging from 7.391×10^{-14} $\frac{\text{ng}}{\text{ion-sr}}$ to 8.828×10^{-14} $\frac{\text{ng}}{\text{ion-sr}}$ over a range of 35° to 80°. When spraying a high energy plume, the yield dropped from 7.304×10^{-14} $\frac{\text{ng}}{\text{ion-sr}}$ to 3.645×10^{-14} $\frac{\text{ng}}{\text{ion-sr}}$ when the polar position of the quartz crystal microbalance was swept from 35° to 80°. These results indicate that the high energy plume produces a secondary plume with less mass than atomic carbon sputtering nickel, but more mass than if the carbon atoms simply bounced off the surface of the target. Results at varying primary energies require further investigation in a more pristine experimental environment to make any statements on the underlying effects.

Acknowledgments

I would first like to acknowledge my adviser, Prof. Josh Rovey, for his mentorship and guidance during my time at the Electric Propulsion Laboratory. Your advising and support were critical to my success as a graduate student and researcher. Thank you to Dr. Deborah Levin, as well as her students Tanapat Bhakyapaibul, Nakul Nawal, and Abhiraj Majumder for their collaboration and patience when explaining their incredible work. Thank you also to Dr. Thomas Liu at NASA Glenn Research Center for overseeing the project. I would also like to thank all of the members of the EPLab that I was lucky enough to work with throughout my graduate career. Thank you to Matt and Chris, for guiding me through my journey with wisdom on electrosprays and material interactions. My sincere thanks to Bryan, Anthony, Allison, and Ally for their camaraderie and collaboration throughout all the hours in the library and the lab. Thanks to Sean, Josh, Nick, and Toyo for their friendship and competition in lab lunch outings and game nights. I would also like to acknowledge all of the staff at UIUC who provided invaluable assistance with the project. Thanks to Kathy Walsh at the Materials Research Laboratory for providing assistance with using the Keyence microscope. Thank you to David Ehrhardt and Peter Kurath at the Advanced Materials Testing and Evaluation Laboratory for their help with understanding material surfaces and polishing test samples. Many thanks to Greg and Dustin in the Aerospace Department Machine Shop for helping with producing experimental fixtures and dealing with constant badgering for quotes. And of course, thank you to Kapton tape, nitrile gloves, and zip ties for holding together my experiments and my sanity. Lastly, thank you to all my family and friends for their constant support and patience throughout the last two years. I could never have gotten even half this far without the people who believed in me and made me believe in myself.

Table of contents

List of Abbreviations

IL	Ionic liquid.
PIR	Purely-ionic regime.
EP	Electric propulsion.
PEEK	polyetheretherketone.
ILIS	Ionic liquid ion source.
QCM	Quartz crystal microbalance.
RPA	Retarding potential analyzer.
HAN	Hydroxylamine nitrate.
C-C	Carbon-carbon.
C-H	Carbon-hydrogen.
SRIM	Stopping and Range of Ions in Matter.

List of Symbols

α	Polar angle, °.
A_{S}	Quartz crystal surface area, cm^2.
C	Mass sensitivity constant, $\frac{\mathrm{ng}}{\mathrm{Hz-cm}^2}$.
d	Distance between thruster and target, cm.
$\frac{\mathrm{d}f}{\mathrm{d}t}$	Frequency change rate $\frac{\mathrm{Hz}}{\mathrm{s}}$.
I_{tar}	Current measured at the target, μA.
$m_{\mathrm{[EMIM]}}$	Mass of an [EMIM] monomer, amu.
m_{C}	Mass of an carbon atom, amu.
$\mathrm{KE}_{\mathrm{[EMIM]}}$	Kinetic energy of an [EMIM] monomer, amu.
KE_{C}	Kinetic energy of an carbon atom, amu.
$\frac{\mathrm{d}m}{\mathrm{d}t}$	Mass deposition rate, $\frac{\mathrm{ng}}{\mathrm{s}}$.
r	Distance between target center and quartz crystal microbalance, cm.
t	Time, min.
V_{em}	Emitter voltage, V.
V_{ex}	Extractor voltage, V.
V_{pri}	Primary plume voltage, V.
q	Charge on particles, C.
y	Differential secondary mass flux yield, $\frac{\mathrm{ng}}{\mathrm{ion\text{-}sr}}$.

Chapter 1

Introduction

This thesis presents work regarding efforts to measure the secondary mass flux yields from a surface impinged on by an electrospray plume. Chapter 1 covers the motivation behind the research, including an overview of electrospray propulsion and plume-surface interactions, as well as a brief review of literature relevant to both topics. In Chapter 2, the experimental approach undertaken to investigate the subject is detailed and all experimental apparatus used in the experiments are described. Results obtained to answer the primary research questions are presented and analyzed in Chapter 3. Chapter 4 discusses the results in context with established science in the field of materials science and electric propulsion. A summary of the study is provided in Chapter 5, along with a brief consideration of limitations of this research as well as potential future directions for the research.

1.1 Electrospray Propulsion

The basic principle of electrosprays is the application of a strong electric field to a meniscus of a conductive liquid. The resultant imbalance between the electrostatic force and the surface tension of the bulk liquid results in a deformation of the liquid interface referred to as a Taylor cone [1]. The focused electric field at the peak of the Taylor cone produces a forced jet of electrified propellant due to the singularity of the field at the liquid-vacuum interface [2]. The electro-hydrodynamic instabilities inherent to the jet in the field free-region results in the expansion of the jet into a plume of droplets, clusters, or individual molecules. There have been a wide range of applications for electrospray technology since its initial development. Manufacturing methods such as electrospinning and thin film deposition have made use of electrosprays to create unique structures and surfaces [3], [4]. Material analysis has been improved by electrospraying macroparticles for mass spectrometry [5]. This thesis will be dedicated to analyzing the applications of electrospray technology

for spacecraft propulsion.

Electrospray thrusters are a type of propulsion system which electrostatically extract and accelerate charged droplets, clusters, or ions of ionic liquid (IL) propellants from "emitters" to high speeds in order to produce thrust. Initially focusing on the emission of large droplets, early development throughout the 1960s and 1970s was interested in using electrosprays as the primary in-space propulsion device for spacecraft [6]. Later efforts starting in the late 1990s and early 2000s were dedicated to utilizing electrosprays for attitude correction and disturbance mitigation for space observatories and small spacecraft [7], [8]. This application of electrospray propulsion hinges on high specific impulse rather than high thrust-to-power. As such, the desired mass of emitted species — or rather mass-to-charge ratio — will be low as possible. The ideal thruster for this purpose emits exclusively singly charged monomers of ionic liquid propellant; this is what is referred to as the "purely-ionic regime" or PIR.

State-of-the-art electrospray propulsion research has primarily focused on three emitter designs: capillary, externally wetted, and porous emitters. See Fig. 1.1 for simple diagrams of each common configuration.

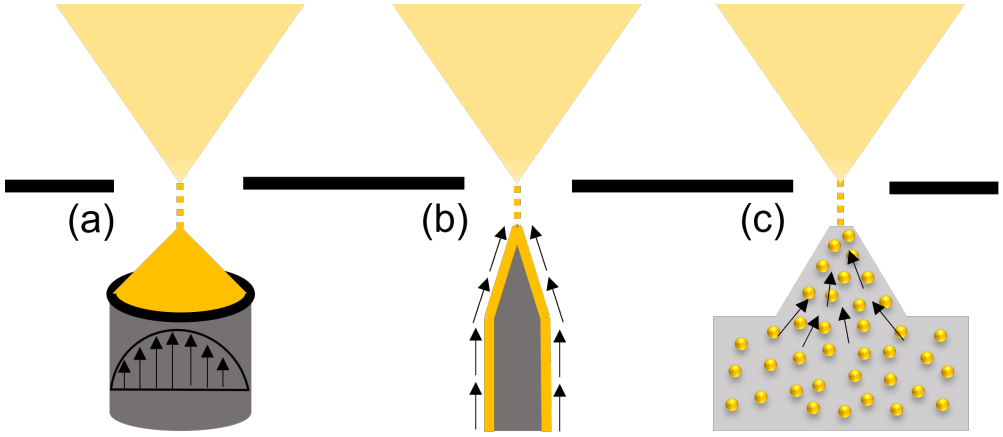

Figure 1.1: Electrospray configurations with (a) capillary emitter, (b) externally wetted emitter, and (c) porous emitter

The most widely investigated configuration, the capillary emitter, consists of pressurized hollow microtubes connecting a reservoir of propellant to a series of exit channels. The exposed liquid at the exit channel is placed under the electric field to form the Taylor cone and emit charged particles [9]. A version of a capillary emitter type thruster designed and built by Busek was launched aboard the LISA Pathfinder spacecraft for in-space demonstration of the technology [10]. Actively-fed capillary emitters tend to emit large droplets and operate at a high thrust-to-power-ratio when compared to other electrospray systems [11]. Although fairly reliable, a number of challenges present themselves with capillary electrosprays. Propellant must be actively forced to the exit apertures of the thruster, requiring a feed system which contributes considerable mass and complexity to the system. Clogging and bubble-formation in the propellant feed lines are also concerns for

the performance and lifetime of these thrusters.

The externally wetted emitters feature solid emitters formed and etched to feature a rough external surface and a curved or conical tip [12]. The liquid propellant wicks up the surface of the emitter to the tip, where the applied electric field forms the Taylor cone and extracts charged particles of propellant. Externally wetted emitters have been shown to be useful in a number of fundamental electrospray studies due to their ease of use in lab settings [13], [14]. They are shown to emit in a nearly PIR mode, but prove to be more difficult to array due to a decrease in wettability when many rough surfaces were placed in any high density array. These thrusters also feature a limited selection of propellants due to the low vapor pressure required for propellant not to evaporate off of the emitter surface in vacuum environments [15].

Porous emitters have gained recent interest for their balance of manufacturability and complexity when compared to capillary and externally wetted emitters. Conical or pyramidal structures are etched from a porous material or extruded with a designed porosity in arrays of tens or hundreds of emitters. An ionic liquid propellant is fed into the pores of the material and wicked to the sharp tips of the emitters by capillary forces. The propellant seeps from the pores and clings to the outer surface of the tips when the electric field is applied, forming a Taylor cone and emission site. Porous emitter thrusters are of particular interest due to the advantages they pose over the proven capillary emitter thrusters from a design perspective. Porous emitters enable capillary driven passively fed propulsion that does not require the mass or complexity of a feed system [16], [17]. This class of thrusters has also been shown to operate closer to PIR than the droplet-heavy capillary emitter thrusters [9].

1.2 Plume-surface Interactions

As mission lifetimes and the complexity of mission requirements have increased with the expansion of commercial space and advancement of scientific exploration vehicles, the demand for electric propulsion has increased significantly. The increased application and reliance on EP devices necessitates that the propulsion systems be accurately and precisely predicted, tested, and evaluated to characterize their capabilities. Much attention has been paid to the tests and analyses that are critical for preparing the systems for in-space performance. The first-principles models essential for predicting key performance parameters further rely on empirical data to enhance the accuracy of their results. As a result, the results from terrestrial facilities must be entirely understood and assessed with proper context and compensation for the effects of the interactions between the thruster and its test environment. Given that a majority of electrospray diagnostics involve directly receiving the plume of charged species on electrical measurement devices or pressure sensors, the interactions between the plume species and the experimental surfaces must be taken into account. Facility

effects have been and continue to be thoroughly studied for existing and proven EP technologies like Hall thrusters due to their sensitivity to background pressure and the impacts of electrical coupling on the thruster plasma. Conversely, electrospray facility effects have only recently come under intense scrutiny from the community.

Beyond the effects of ground-based testing, EP systems may pose a threat to their spacecraft if their interactions with other subsystems are not fully considered. Of utmost concern for electrospray spacecraft interactions are spacecraft charging and plume impingement [18]. The charged particles emitted by the thruster can return to the spacecraft, resulting in spacecraft charging and potential material erosion. The liquid-phase propellant and its conductivity also present several further risks, as plume interception on spacecraft surfaces will not only result in spacecraft charging and surface removal, but chemical contamination as well [19]. Beyond these primary interactions, any surface impinged on by the plume will also be a potential site for the production of secondary species.

The purpose of this work is to develop a method for measuring the mass of secondary species produced by a primary electrospray plume impinging on a downstream surface. Previous work from the EP community has made progress in characterizing the emission of secondary charged species in electrospray material interaction [13], [20], [21]. Previous work has also attempted to characterize sputtering yields from bombardment by electrosprayed droplets rather than ion plumes [7], [22], [23]. However, potential secondary species include electrons, atomic and molecular ions, clusters, nanodroplets, as well as neutral pairs of deposited propellant or sputtered material from the impinged surface. The mass of these species and their angular distribution should be understood in order to understand potential facility effects arising from the deposition of secondary mass on experimental instruments. These results can also be used in attempts to improve existing models of plume-surface interactions and their consequences with regards to facility and spacecraft interactions.

1.3 Secondary Mass Flux

In discussing the production of the secondary mass, the typical materials science terminology such as sputtering assumes more about the primary-secondary collisions than can be surmised at this stage of investigation. To refer to the measurements made in this study as the sputtering yield would assume that all measured mass is target material etched away from the topmost layers of the surface. However, results from the studies cited in this chapter indicate that a significant amount of charged species are reflected, scattered, or otherwise removed from the surface of the target and ejected back into the facility as part of the secondary plume. Therefore, this study will refer to secondary mass flux yield as the mass per incident ion rather than atoms per incident ion.

Chapter 2

Experimental Approach

2.1 Porous Glass Thruster

The electrospray source used in these experiments was a porous glass electrospray thruster designed at UIUC based on the AFET-2 design from the Air Force Research Lab at Edwards Air Force Base [17]. Manufacturing, assembly and loading procedures described by [24] were used in preparing the thruster for all experiments. The emitter array was manufactured from a 2.5 mm thick, 20 mm diameter P5 porous glass filter disk using a diamond edged grinding wheel. Each emitter is a square pyramid, with a height of ∼250 μm and an aspect ratio of ∼0.7. The 20 mm diameter disk allows for a 24 x 24 array of emitters with a pitch of 576 μm. Figure 2.1 shows a porous glass disk in the manufacturing assembly.

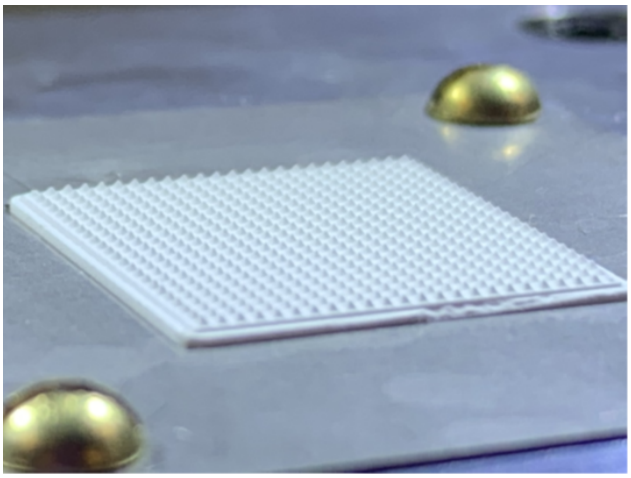

Figure 2.1: Ground emitter disc

The extractor array was designed to match the pitch and offset measured from a set of machined emitters.

Using a RMI EF-20 laser engraver, the array pattern was cut into a flattened sheet of 0.004" thick aluminum shim stock. To ensure flatness and provide structure to the extractor grid, the cut array was then bonded to a steel frame using a conductive silver epoxy.

The other components of the thruster were milled and machined using conventional machining techniques, with 0.001" tolerances on all measurements. With all components prepared, the thruster could be assembled, starting with the propellant module, which contains the emitter, propellant, reservoir, and contact spring. The propellant module housing is machined from a piece of polyetheretherketone (PEEK). A disc spring sits at the bottom of the module, with a 2.5 mm thick, 20 mm diameter P4 porous borosilicate filter disk sitting on top of the spring. The P4 disk acts a reservoir to contain excess propellant. The machined emitter disk is then placed over the propellant reservoir, with a sheet of filter paper between the two disks to regulate the flow from the reservoir to the emitter array. A steel electrode frame was then bolted down over the edges of the emitter array, compressing the spring and pushing the entire assembly together. The propellant module was bolted into the aluminum thuster housing with a 0.004" thick sheet of aluminum shim stock placed between the bottom of the thruster housing and the propellant module to set the emitter array at the desired height. The extractor was finally placed over the emitter array and aligned over the tips using an optical microscope at 20x magnification. Figure 2.2 shows a fully assembled thruster.

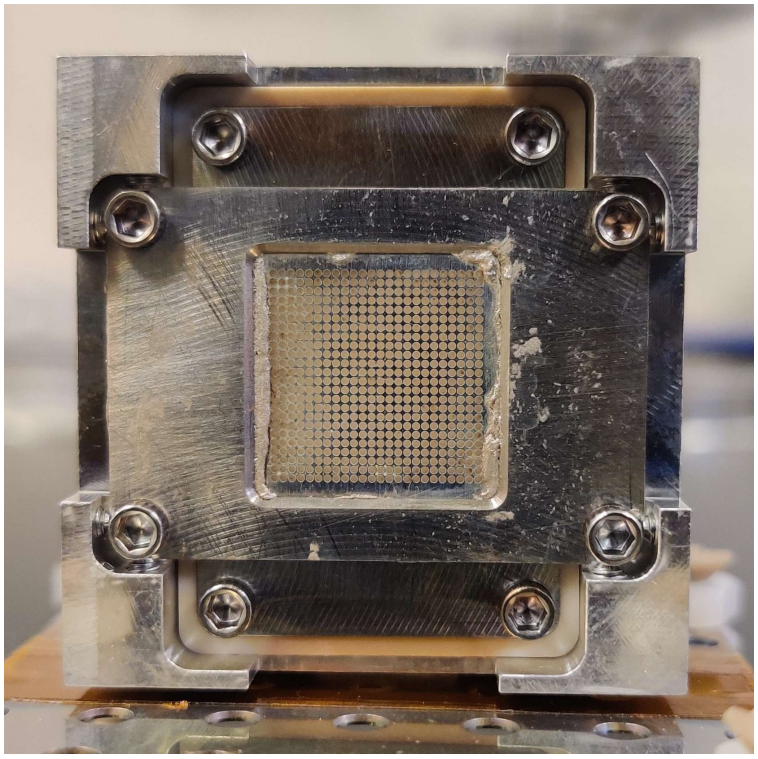

Figure 2.2: Porous glass thruster, assembled and loaded with [EMIM][BF_4]

To verify the emitter alignment and quantify the gap distance between the emitter tips and the extractor, the assembled thruster was analyzed under a Keyence VKX1000 Laser Confocal Microscope. See Figure 2.3 for imaging and profiling steps in the assembly process. An emitter-extractor gap between 50 μm and 150 μm was deemed acceptable when preparing a thruster for testing [24].

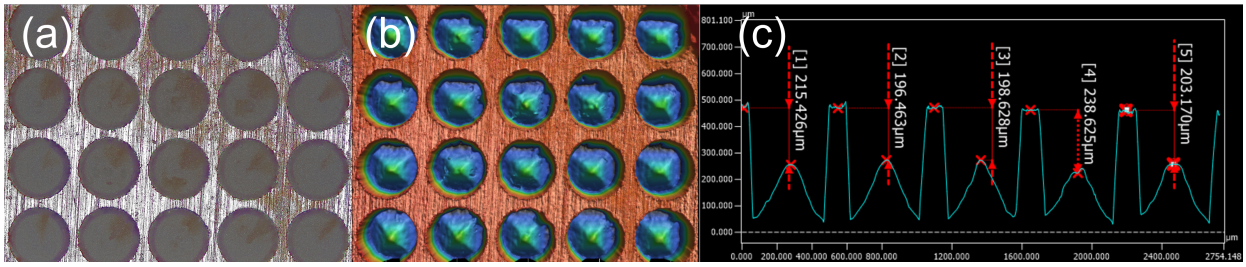

Figure 2.3: (a) Overlaid laser and optical image of 5 x 4 section of thruster array, (b) height map of the same section, and (c) height profile of one row of emitters

Thruster loading took place after the assembly and verification. To fill the propellant reservoir and emitter array with propellant, an access hole was machined into the rear of the thruster housing and the propellant module. The thruster rested upside down while drops of propellant were dripped directly onto the propellant reservoir. Approximately 0.6 mL of propellant could be deposited into the propellant housing before the emitter array flooded. To ensure that propellant had seeped to the tips of the emitter array, the thruster was left upside down for approximately two hours. The entire loading and saturation process took place in a purged dry air glove box to minimize the effects of background humidity on the propellant. See Fig. 2.4 for detail on the propellant loading process.

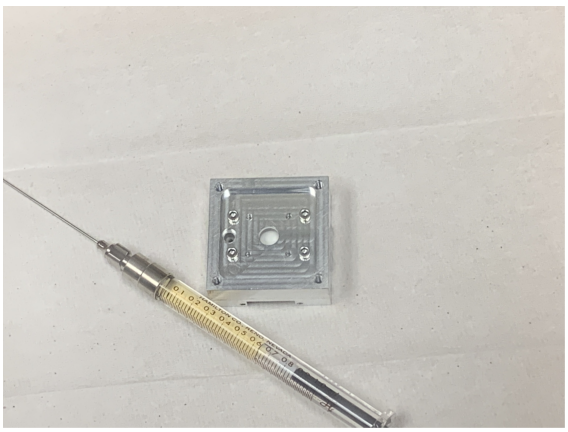

(a) Empty thruster ready for loading and 1 mL syringe filled with [EMIM][BF_4]

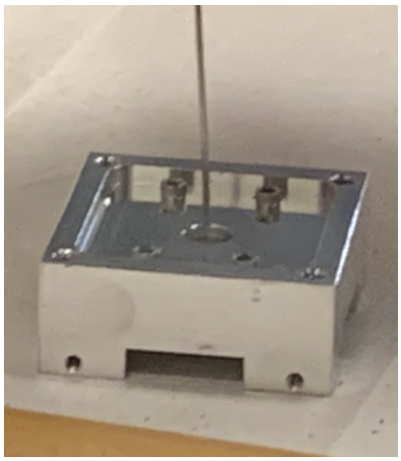

(b) Thruster filling using luer lock syringe

Figure 2.4: Loading procedure for porous glass thruster

1-ethyl-3-methylimidazolium tetrefluoroborate ([EMIM][BF_4]) was chosen as the ionic liquid ion source

(ILIS). This particular propellant has been demonstrated as a easy-to-use, cost effective, and versatile propellant in a number of electrospray applications in lab tests [17], [21], [24]. After loading with propellant, the insulation of the thruster was validated using a Megger high voltage tester. The extractor was held at ground while the emitter was swept from 0 to 500 V. With propellant saturated to the emitter tips, an impedance greater than 100 GΩ and leakage current less than 10 nA at 500 V was determined to be acceptable for thruster testing.

2.2 Quartz Crystal Microbalance (QCM)

A quartz crystal microbalance (QCM) is a piezoelectric device commonly used as a monitoring device in thin-film deposition applications [25]–[27]. The working principle of a QCM is that the resonant frequency of a cut piece of quartz crystal is correlated to the thickness of the crystal. As the thickness of the resonant material of the crystal increases, the fundamental frequency will decrease proportionally to the added mass of the uniform film on the crystalline surface. By applying a driven frequency to the crystal, the measured frequency change can be used to calculate the amount of mass per unit area that has been deposited over time. See Equation (2.1) for a mathematical representation of this relationship, referred to as the Sauerbrey equation.

$$\frac{\mathrm{d}m}{\mathrm{d}t} = -CA_{\mathrm{s}}\frac{\mathrm{d}f}{\mathrm{d}t} \tag{2.1}$$

In this expression, $\frac{\mathrm{d}f}{\mathrm{d}t}$ is the measured frequency change, A_{s} is the surface area of the crystal resonator upon which mass is being deposited, and C is the mass sensitivity constant, which describes the degree to which a mass deposition per unit surface area perturbs the crystal frequency. This sensitivity constant is determined by the manufacturer by depositing a known mass per unit area on a representative sample of crystals and measuring the frequency change from its resonant value.

The piezoelectric element of the QCM is known to be highly sensitive to changes in temperature [28]–[30]. For these experiments, the QCM was not operated with any form of cooling. Typical QCM cooling systems run fluid around the body of the oscillator to maintain the temperature of the sensor. As secondary species from plasma and ion bombardment generally have low energy, and the amount of expected flux was relatively low, cooling was deemed unnecessary as the power deposition from secondary mass flux would be negligible [31].

The QCM used in these experiments was an Inficon front load sensor monitored by an XTC/3S Deposition

Controller with an external oscillator. The deposition controller measures the frequency with a frequency resolution of 0.001 Hz and a time resolution of 1 s. Inficon Gold-Coated 6MHz quartz crystals were used as the receiver for their superior adhesion when compared to bare quartz crystals or alloy-coated crystals. The exposed area of the crystal was measured to be 1.593 cm^2 when loaded into the sensor head. Figure 2.5 shows the QCM with a fresh gold-coated crystal prior to any deposition.

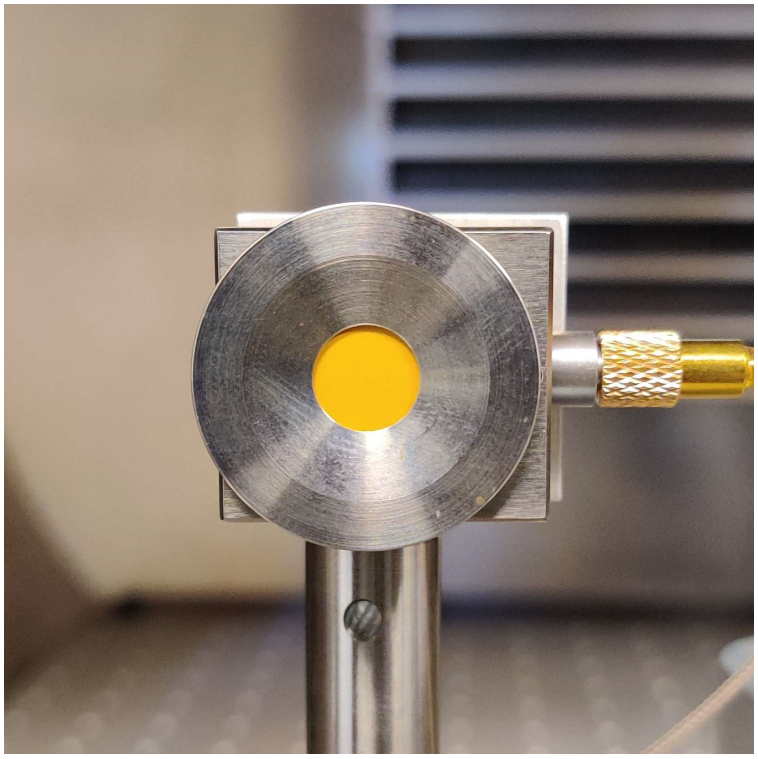

Figure 2.5: Inficon quartz crystal microbalance, with gold-coated 6 MHz quartz crystal

The XTC/3S and external oscillator provided the driving frequency for the QCM and measured the change in resonant frequency during deposition. The monitor had a time resolution of 1 second and a frequency resolution of 0.028 Hz.

2.3 Experimental Setup

The experimental approach utilized for the tests treated secondary mass flux as a deposition process which could be monitored by a QCM like any other deposition process. A similar approach was undertaken by Williams et al. to measure mass sputtered from a material surface by a xenon beam using a rotating QCM [26]. Figure 2.6 shows a schematic of the test setup as envisioned, based on the xenon beam sputtering experimental design.

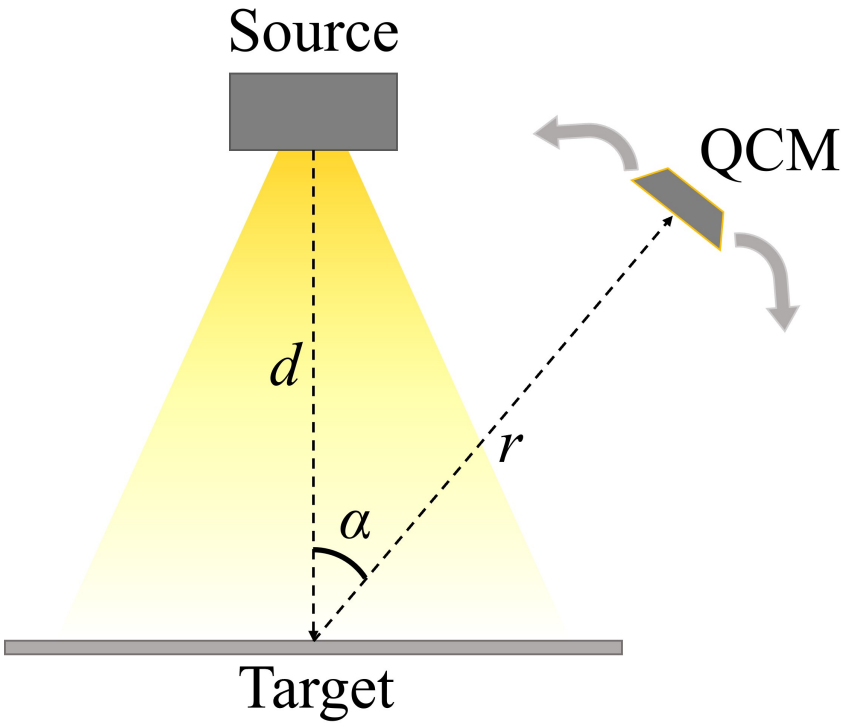

Figure 2.6: Schematic of Experimental Setup

Figure 2.7a shows the proposed experimental setup implemented in the facility. The thruster was fixed at a position $d = 12$ cm away from a fixed 6" x 6" nickel target with the extractor face and nickel surface parallel to one another. The QCM was placed on a rotating arm $r = 12$ cm away from the center of a target, such that the polar angle defined by the target normal and the QCM normal could be swept in the range of $\alpha \in [35°, 90°]$. The nickel surface was intentionally chosen as the bombardment target due to its prevalence in facility and spacecraft environments, as well as its relative simplicity when compared to other common materials such as aluminum and steel. Those materials are alloyed and composed of a variety of materials, whereas a polycrystalline nickel target is a single homogeneous surface.

High voltage connections were placed on the emitter and extractor connection points in order to operate the thruster. With the use of Texas Instruments AMC1311 isolation amp evaluation modules, the current across these high voltage lines was measured at all times. Plume current received at the target was measured by a Keithley 6514 electrometer operating in ammeter mode operating in a range of ± 200 μA. This instrument provides an accurate measure of small currents with resolution of 0.01 nA. See Fig. 2.7b for the high voltage connection points on the thruster and target surfaces.

The radial position of the QCM was decided to be $r = 12$ cm in order to limit the probability of the primary plume impinging on the sensor and influencing mass measurements. Figure 2.7c shows this separation

between the exterior face of the thruster and the primary sensing surface of the QCM.

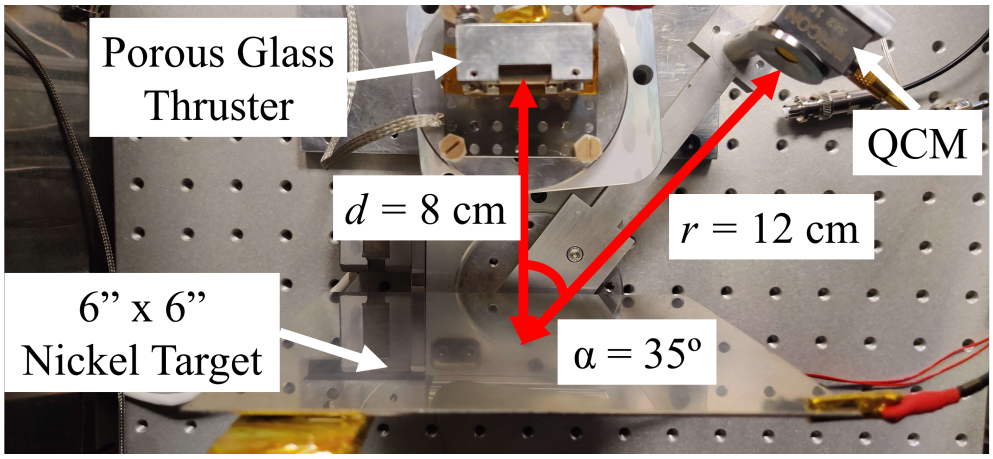

(a) Top-down view of setup

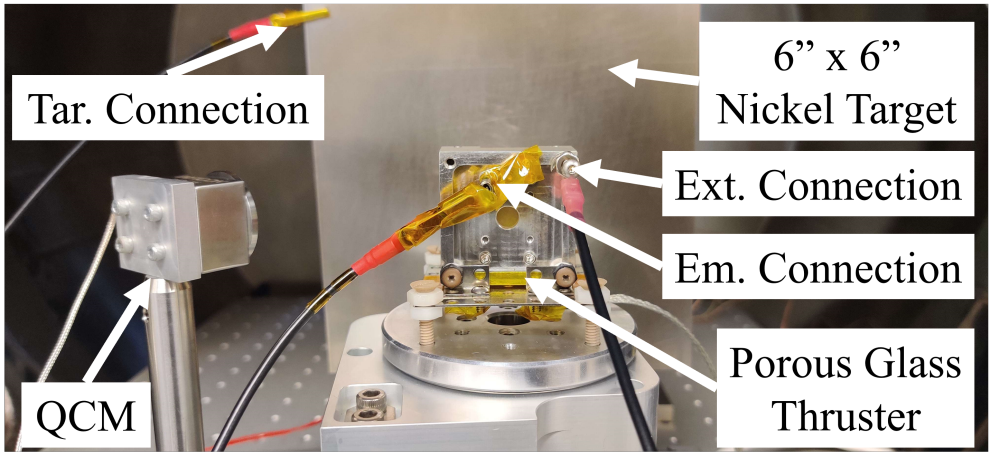

(b) Rear view of setup

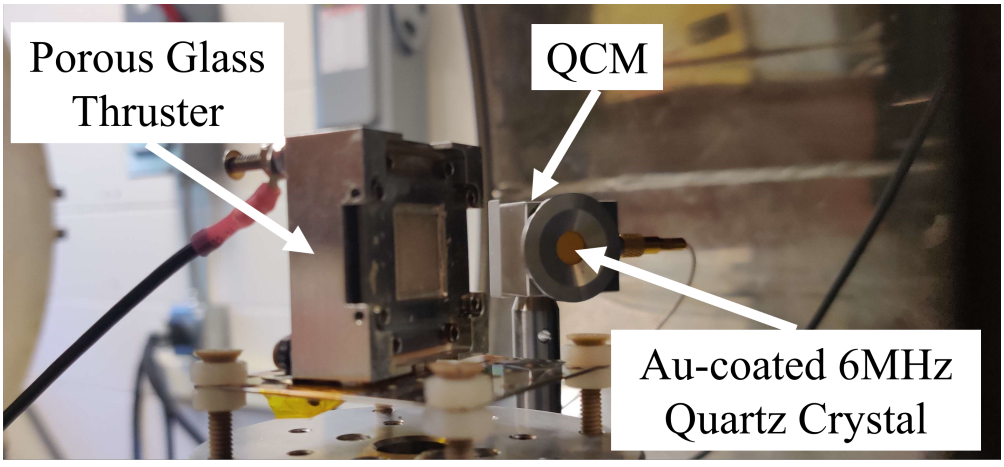

(c) Reverse angle view of setup

Figure 2.7: Experimental setup for measurements of secondary mass flux

2.4 Facility

Experiments were conducted in a belljar vacuum chamber with a depth of 27" and a diameter of 24". The chamber was equipped with a Leybold DB16 rough vacuum rotary pump and a CTI CryoTorr 8 cryopump driven by a Brooks 9600 helium compressor. The chamber is monitored by a convection enhanced Pirani gauge at low vacuum and a hot filament ion gauge at high vacuum. In this configuration, the chamber had a measured base pressure of 6×10^{-6} Torr.

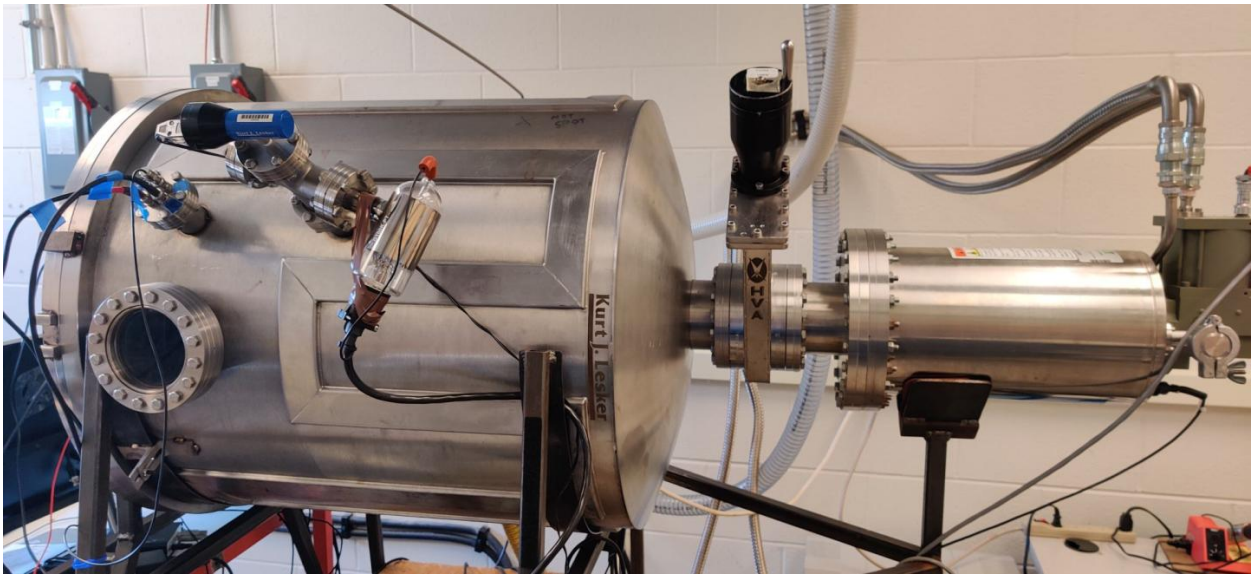

Figure 2.8: Belljar vacuum chamber with cryopump and vacuum monitoring instruments shown

Chapter 3

Results and Analysis

3.1 Thruster Characterization

In order to provide any assessment of the secondary plume, the primary plume must first be assessed and characterized. Recent work from the University of Illinois provided a comprehensive characterization of the porous glass thruster operating with different propellants, including [EMIM][BF_4] [24]. Measurements collected in that survey included I-V curves, retarding potential curves, and time-of-flight spectra. For the purposes of these experiments, characteristic curves of thruster voltage and current as well as RPA measurements were collected to compare the plumes and get insight into the properties and composition of the ion plume.

Figure 3.1 shows I-V curves for the thruster operating in cation and anion modes. These curves were collected by fixing the extractor potential at ground, and sweeping the emitter bias from 0 V to 2000 V in a 1 Hz triangle wave.

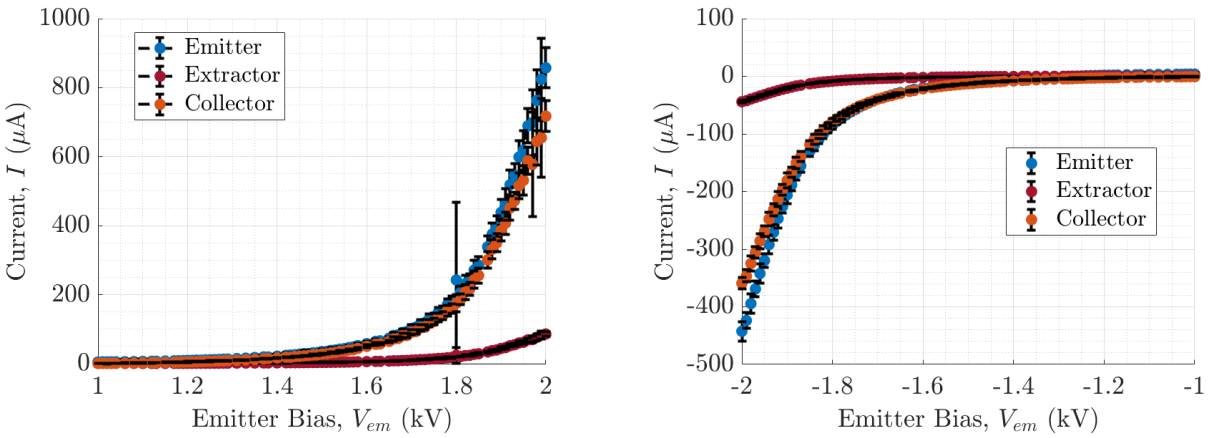

(a) Positive Operation

(b) Negative Operation

Figure 3.1: Porous glass thruster I-V curves

Note that the onset voltage appears to be ∼1300 V for cation operation and ∼-1450 V for anion operation. Typical of similar bipolar electrospray systems, the anion current was markedly lower than the cation current. Results from other electrospray users demonstrate onset voltages ranging from 900 V to 1500 V, and a broad range of emission, collection, and impingement currents [11], [17], [24]. These exact performance characteristics will be heavily dependent on the specific dimensions of the thruster and the alignment of the emitter and extractor [8].

The energy distribution of the primary plume was assessed using a conventional three-grid retarding potential analyzer (RPA). The RPA features a simple Faraday cup, with a series of biased grids in front of it. When collecting these curves, the centerline of the ion plume was oriented colinear to the centerline of the Faraday cup. The first grid the encountered by ions in the plume was held at ground to limit the effects of the downstream grids on the plume prior to entering the analyzer. The middle grid was swept between high negative and high positive voltages to retard the motion of incoming ions. The last grid was held at -60 V in order to reject secondary charged species produced by impacts between plume ions and grid surfaces. These curves reveal the energy distribution of the primary plume ions based on their stopping energy. This offers an estimate for the energy with which primary ions will strike a downstream surface. Figures 3.2a and 3.2b shows the cumulative RPA spectra for a positive and negative primary plume, respectively. The emitter bias was ±1900 V, while the full scale retarding potential was ±2000 V. The x- and y-axes were normalized such that $x = 1$ represents a retarding voltage of 2000 V and $y = 1$ is the maximum signal measured at the Faraday cup.

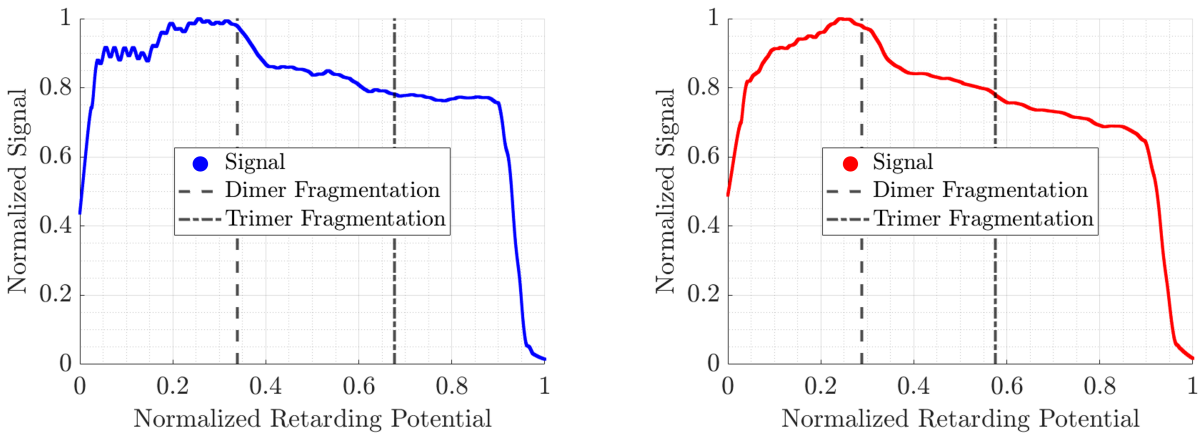

(a) Positive Operation

(b) Negative Operation

Figure 3.2: Porous glass thruster RPA curves

The figures show the increasing signal at low suppression voltages in both spectra. Similar behavior was seen in RPA spectra obtained by Bruno et al. in recent studies characterizing electrospray thrusters with [EMIM][BF_4] and several hydroxylamine nitrate (HAN) based propellants sprayed with an iEPS porous glass thruster [32]. The positive signal demonstrates drops at ∼0.35 and ∼0.62, corresponding to expected fragmentation of $[EMIM]^+$ dimers and trimers. Similarly, the negative signal exhibits drops at ∼0.32 and ∼0.6, which close match the fragmentation energies for $[BF_4]^-$ dimers and trimers. These cumulative signals show strong agreement with previous results from an identical porous glass thruster operated at UIUC in Ref. [24], as well as similar porous glass thrusters [11], [17].

3.2 QCM Characterization

QCMs are well-characterized instruments used commonly in a variety of thin film deposition systems for measuring and monitoring purposes. For these experiments, no mass calibration was conducted using a known mass deposition source; instead, the mass sensitivity constant given by the crystal manufacturer ($12.35\ \frac{ng}{Hz-cm^2}$) was used for mass determination [28]. Additional characterization was completed to assess the instrument's performance in this particular experimental setup and design the experimental procedure to best accommodate the sensor's functionality and produce repeatable results.

3.2.1 Background Drift in Vacuum

The QCM frequency was observed in the ambient background vacuum conditions under which the deposition experiments would be conducted before monitoring any deposition processes using the sensor. Figure 3.3

shows two traces of the QCM frequency over several hours of operation.

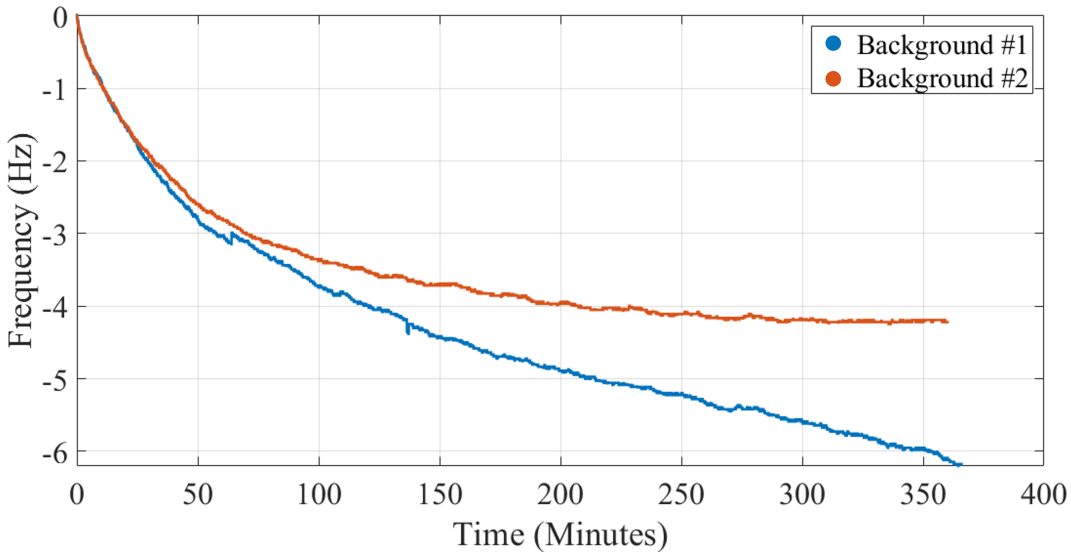

Figure 3.3: QCM frequency reading in vacuum background

Both traces initially exhibit a steep decrease in frequency, with a decaying rate of change over the observation period. In the first background measurement, the rate appears to reach a steady state of approximately 6.89×10^{-3} $\frac{\text{Hz}}{\text{min}}$. The second background measurement exhibited a similar initial rate of decrease, but instead leveled off to a relative steady state with no change in frequency for the last two hours of observation. The residual rate of decrease was attributed to thermal effects and minor temperature fluctuations ($< 2°$C) of elements in the chamber, resulting in a low level of frequency drift. To determine the extent that this background drift could influence measurements of deposited mass, initial deposition tests were conducted at constant thruster voltage and constant QCM position.

3.2.2 Uniform Deposition Tests

The goals of performing deposition at uniform conditions were a) demonstrating that results from the QCM are repeatable and reliable and b) comparing temperature-related drift rates to deposition rates and show that error due to thermal conditions is relatively small.

In these initial experiments, the QCM's polar position was fixed at 35°. Three deposition events were conducted in a single chamber pump-down with the same QCM crystal. In each deposition, the primary plume impinging on a nickel target was produced by the same porous glass thruster operating with a grounded extractor and the emitter biased to ±1900 V. The thruster was operated in a 1 Hz square wave bipolar mode to ensure maximum operating time, as previous tests with the thruster in monopolarity showed a sharp

decline in primary plume current over time and a propensity for shorting and arcing between the emitter and extractor. Each deposition took place over 60 minutes, and 60 minutes of "settling" time was taken in between each deposition phase to allow the QCM to reach a steady state after each deposition. Figure 3.4 shows the frequency traces from each test with traces before and after the deposition phase included.

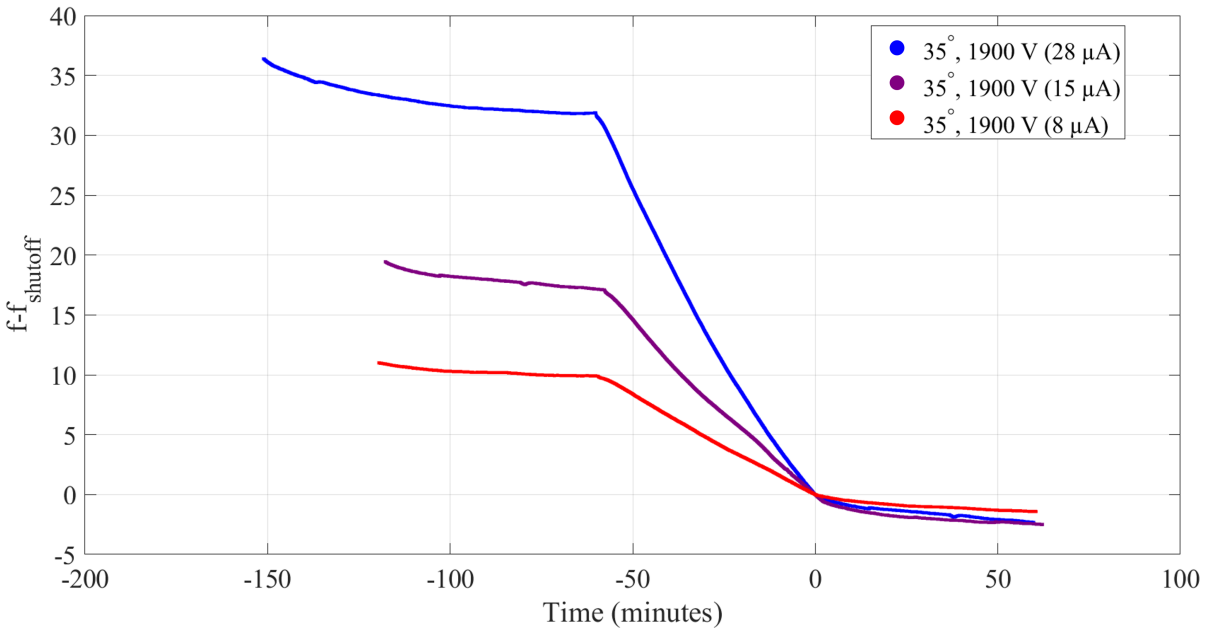

Figure 3.4: Raw measurements of QCM frequency vs time, with end of deposition set to $f = 0$ Hz and $t = 0$ min

Note that the first test — indicated in blue — features 90 minutes of pre-deposition data. The QCM was turned on and left to reach a relatively steady state, as determined by the results from tests detailed in Ch. 3.2.1. Time at $t = 0$ was set as the time at which the thruster was shut off to better compare the deposition phase for each test. Note that the average current in each test — indicated in the legend — decreased in each sequential deposition. Despite operating in the safer bipolar mode, the thruster output decreased over time, which likely caused the variance in frequency rates during the deposition phase. To better compare these deposition events and calculate the mass deposition yield, these events were normalized by the current impinging on the target at each time interval. Prior to that comparison, however, the pre- and post-deposition frequency rates were calculated and compared with the frequency rate during the deposition. Pre-deposition time was defined as the 30 minute period before the thruster was turned on, while post-deposition starts 30 minutes after the thruster had been turned-off and ends the moment the next deposition process was started. The frequency rate $\frac{\mathrm{d}f}{\mathrm{d}t}$ was calculated over each 1 second interval and averaged over the time span for each defined phase of the test. The percent error was calculated for the post-deposition relative to the

pre-deposition drift rate. The relative magnitude of the pre- and post-deposition frequency rates compared to the average frequency rate during deposition was also calculated. Table 3.1 presents the calculated frequency rates for each of these phases of the tests.

Table 3.1: Frequency change rates and relative error for tests at constant energy and constant angle

	Deposition	Pre-Deposition		Post-Deposition		
Test #	$\frac{df}{dt}$ ($\frac{\text{Hz}}{\text{min}}$)	$\frac{df}{dt}$ ($\frac{\text{Hz}}{\text{min}}$)	% Depositon	$\frac{df}{dt}$ ($\frac{\text{Hz}}{\text{min}}$)	% Deposition	% Error
1 (28 μA)	-0.5313	-0.0104	1.958	-0.0276	5.204	165.7
2 (15 μA)	-0.2955	-0.0276	9.356	-0.0115	3.891	58.41
3 (8 μA)	-0.1631	-0.0115	7.050	-0.0138	8.456	19.94

Note that the relative error was fairly high for all tests and ranged from 19.94% to 165.7%. However, the drift rates for both pre- and post-deposition in all cases was fairly small, ranging from 1.958% to 9.356%. The inconsistent background drift rate indicates that the deposition event may affect the background drift for some time after the deposition has ceased, but the relatively small magnitude of the drift indicates the thermal effects may not be significant enough to cause irreparable uncertainty in measurements. The deposition frequency was "corrected" by simply subtracting the linear frequency rate attributable to the pre-deposition drift. Figure 3.5 shows the frequency measurements with the pre-deposition drift removed, with $t = 0$ shifted to the time when the thruster was turned on.

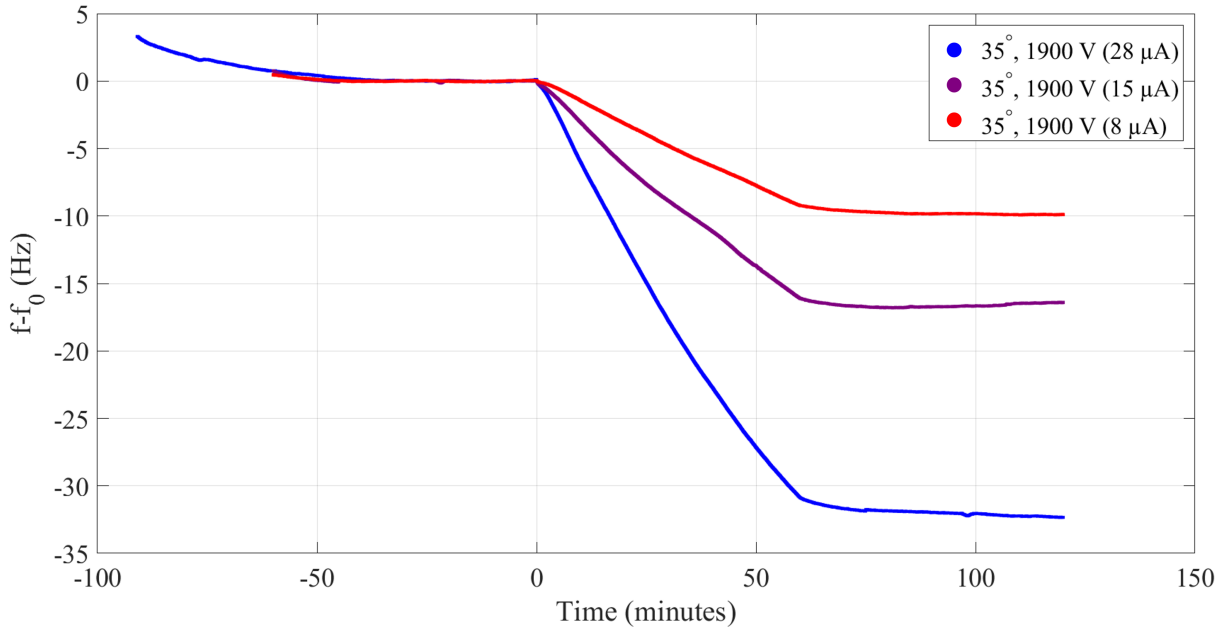

Figure 3.5: Frequency vs time with pre-deposition drift rate removed

When the pre-deposition drift is removed, the deposition phase is not significantly altered, while the post-deposition drift appears lessened for the 28 μA and 8 μA cases. With the drift corrected for, the mass accumulation could then be calculated using the Sauerbrey equation, as described in Ch. 2.2. The cumulative mass deposition $\sum_{t=0}^{t_{\text{off}}} \frac{dm}{dt}$ over time is plotted for each test in Fig. 3.6.

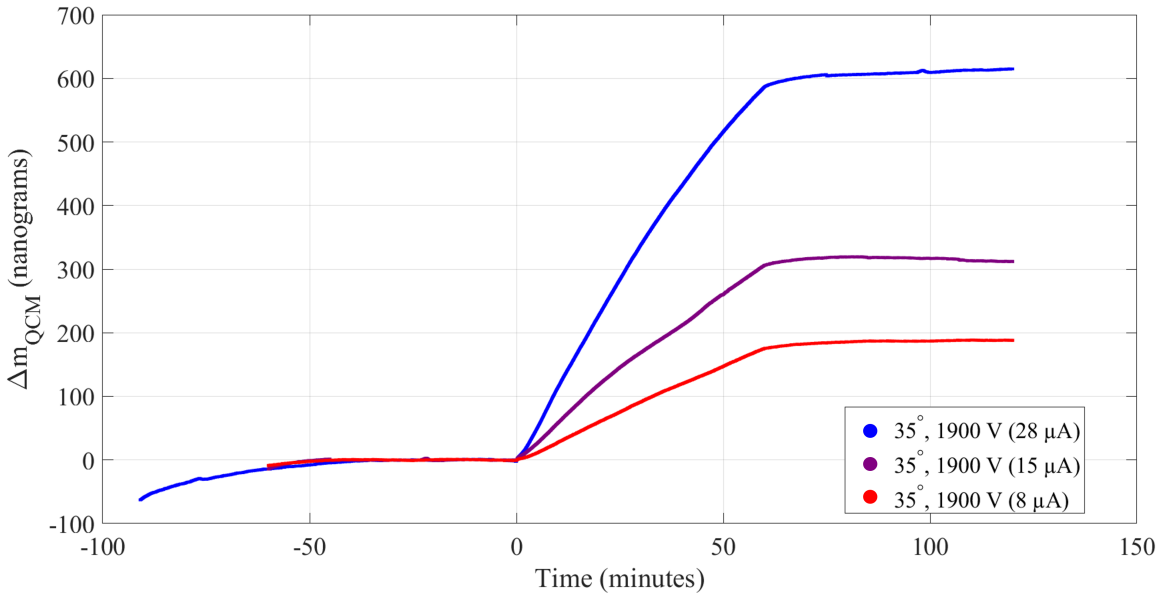

Figure 3.6: Mass deposited on QCM vs time

Before computing the mass flux yields by factoring in the current measurements, the mass deposition results were normalized to compare the deposition phases more directly and demonstrate repeatability in the frequency measurements alone. Dividing the cumulative mass deposited by the mass deposition at the time when the thruster is turned off, the results presented in Fig. 3.7 are produced.

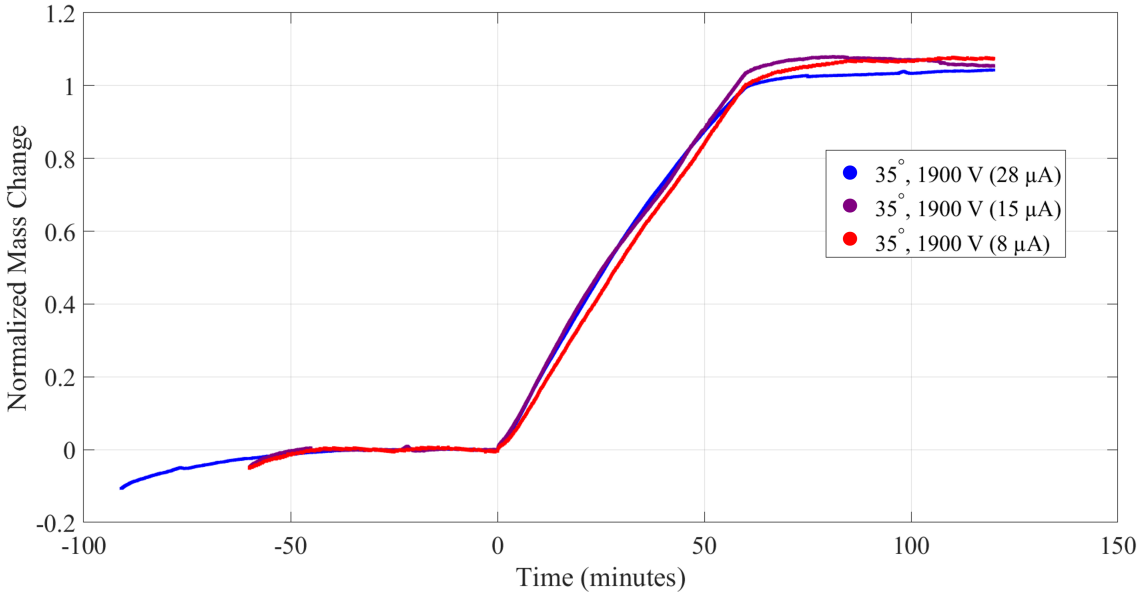

Figure 3.7: Normalized mass deposition vs time

The time scale was then normalized by the time during the deposition phase such that the thruster is turned on at time $t = 0$ and turned off at $t = 1$. See Fig. 3.8 for the frequency results normalized along both axes.

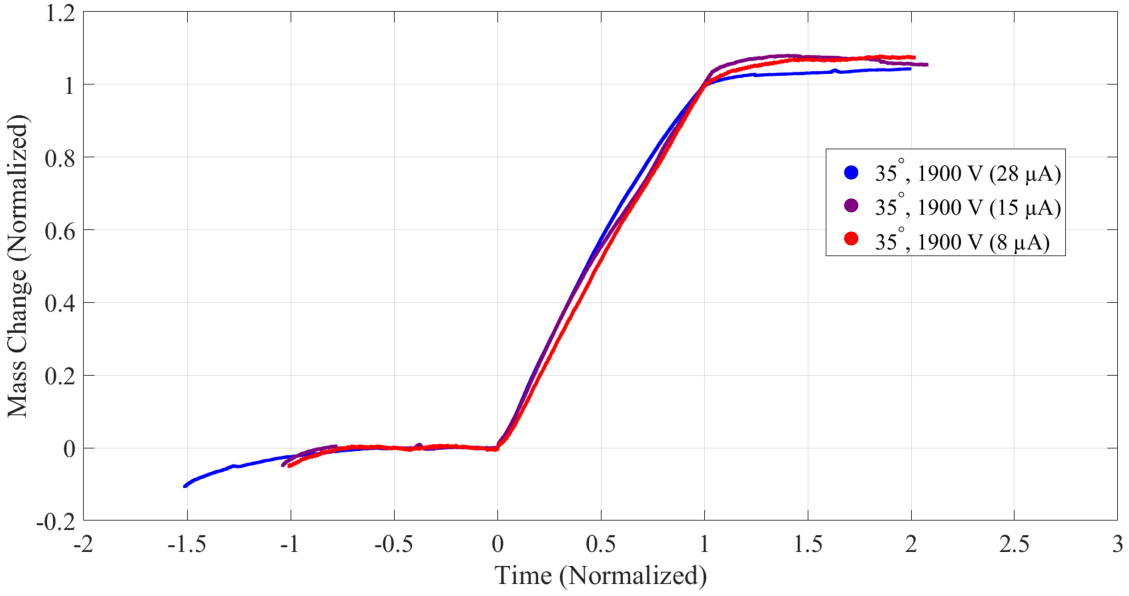

Figure 3.8: Normalized mass deposition vs normalized time

From these normalized results, the deposition rate on the QCM appears uniform across three relatively uniform processes. Calculating the mass flux yield from the mass deposition required factoring in the current

impinging upon the target in order to consider mass ejected per incident charge. See Fig. 3.9 for a snapshot of raw current traces during five seconds of spraying.

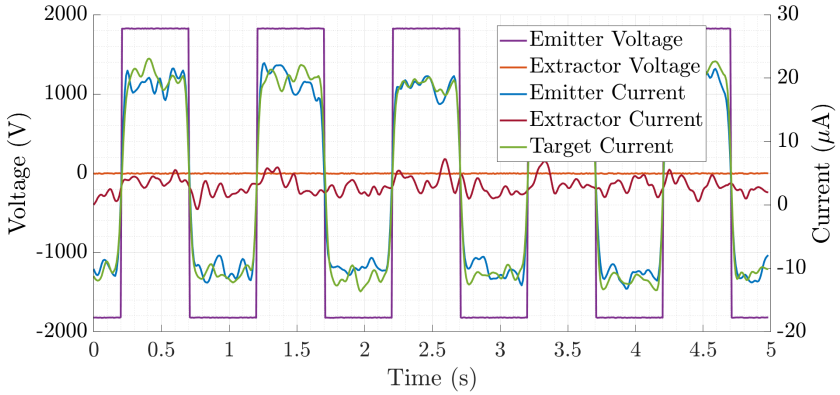

Figure 3.9: Raw current trace from 5 seconds of Test #2 (15 μA)

The raw target current I_{tar} was averaged over each 0.5 second pulse in each polarity. Given that the QCM only logged frequency every one second, the current data had to be further processed to directly compare the two values and calculate a single value for mass flux yield over a given time interval. The pulse-averaged frequency and current data were individually interpolated onto uniform time arrays such that one $\frac{\mathrm{d}m}{\mathrm{d}t}$ data point corresponds to the pulse averaged I_{tar} value at that same time interval. The mass flux yield y was then calculated according to Equation (3.1), which is adapted from the method used in Ref. [26].

$$y = \frac{\frac{\mathrm{d}m}{\mathrm{d}t} q r^2}{I_{\text{tar}} A_{\text{s}}} \tag{3.1}$$

For the purposes of this calculation, the mass deposition rate $\frac{\mathrm{d}m}{\mathrm{d}t}$ is represented in $\frac{\text{ng}}{\text{s}}$, while the current is measured in $\text{A} = \frac{\text{C}}{\text{s}}$. Assuming singly charge species impinging on the surface, the charge per incident particle is $q = e = 1.602 \times 10^{-19} \frac{\text{C}}{\text{ion}}$. To present these results as a solid angular component, recall from Ch. 2.3 that the solid angle will be determined by the ratio of the squared distance between the target center and the QCM r to the sensor crystal area A_{s}. As a result, the differential mass flux yield plotted in Fig. 3.10 is in units of $\frac{\text{ng}}{\text{ion-sr}}$.

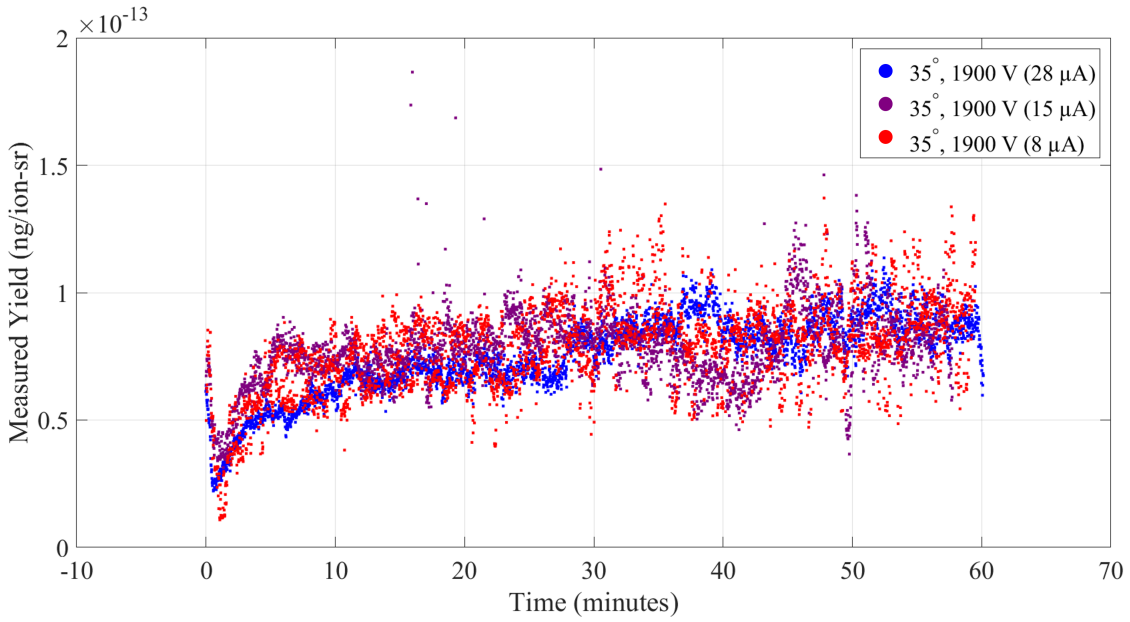

Figure 3.10: Secondary mass flux yield vs time

Note the transience in the mass flux yield values in the first ∼15 minutes of deposition. This transience is likely attributable to a combination of thermal effects and thin film formation. As the secondary particles accumulate on the surface of the crystal, they deposit a small amount of energy onto the sensor and disrupt the thermal equilibrium the sensor was in prior to spraying. Additionally, the film developing on the crystal is not an immediate monolayer. Only when the particles have formed a relatively uniform film covering the total exposed surface area does the resonant frequency of the crystal change proportionally to the mass per unit area. As a result, only the mass flux yields after the transience appears to have settled to a steady state — ∼15 minutes in these tests — are considered representative of the actual values. Table 3.2 presents the average of $\{y|t > 15\,\text{min}\}$ for each of the three deposition tests. Note that values are expressed to four significant figures, as the reported mass sensitivity constant limits the precision with which values can be provided with confidence.

Table 3.2: Average secondary mass flux yields at constant energy and polar angle

Test #	$\lvert y\rvert(\frac{\text{ng}}{\text{ion-sr}})$	$\sigma(\frac{\text{ng}}{\text{ion-sr}})$
1 (28 μA)	7.992×10^{-14}	1.132×10^{-14}
2 (15 μA)	8.017×10^{-14}	1.319×10^{-14}
3 (8 μA)	8.205×10^{-14}	1.157×10^{-14}

The cumulative average and variance for these three yields are then $\bar{y} = 8.07 \times 10^{-14}\ \frac{\text{ng}}{\text{ion-sr}}\ \pm 1.16 \times$

10^{-15} $\frac{\text{ng}}{\text{ion-sr}}$. Given the low cumulative variance in these values, the method was deemed repeatable and further testing applying the process was completed.

3.3 Deposition Studies

The primary goals of this investigation were to study the effects of primary plume energy on secondary mass flux yields and characterize the angular distribution of the secondary mass. The deposition studies detailed below were undertaken to answer those research questions. Each set of deposition studies were completed in a single pump-down with a fresh crystal loaded into the QCM for each new set of tests. In each deposition event, the thruster was operated for at least 30 minutes, with an hour of post-deposition settling time between each sequential test. The thruster was completely cleaned, reassembled, and reloaded between vacuum pump-downs to get the maximum thruster performance for each set of tests. Each step of the analysis is briefly detailed along with the presented results.

3.3.1 Constant Angle, Varying Primary Energy

The main challenge in studying the relationship between secondary mass flux yield and the energy of the primary plume was expanding the operating range of thruster energies. With a grounded extractor, the range of emitter voltages that could produce a reliable plume was very small. Below roughly $\pm$1700 V, the thruster would either not emit a plume or produce current too low to remove enough secondary material in a reasonable experimental time scale. Above approximately $\pm$2400 V, the thruster behavior was erratic, with high impingement current and an increased likelihood for critical failures such as the emitter shorting or propellant arcing to the extractor. The $\sim$700 V range of primary plume energies was deemed too low to generate any useful data regarding the effects on the secondary mass flux yields. To account for this, the extractor was not fixed at ground, but was instead allowed to be biased in a 1 Hz square wave mode in sync with the emitter bias. For example, if the goal was to produce a $\pm$500 V primary plume, but the thruster was producing a stable plume at an extraction potential of $\pm$2000 V, the emitter was biased to $\pm$500 V in a 1 Hz square wave, while the extractor was biased to $\mp$1500 V in a 1 Hz square wave phase shifted by 180° from the emitter square wave. The emitted plume will have a nominal potential of 500 V relative to the grounded target and chamber, but will still be extracted from the thruster as if it was operated in standard conditions.

The polar position in these tests was once again fixed at 35°. Five test points on a range of energies on $V_{\text{pri}} \in [250, 2500]$ V were determined in order to cover an order of magnitude of primary plume energies. Tests were conducted at high voltages first, and decreased in log spaced increments down to the low voltage in each sequential deposition phase. Figure 3.11a shows the frequency traces for the full test range, and Fig. 3.11b

aligns the five tests with $t = 0$ set to the time at which the thruster was turned off after each deposition.

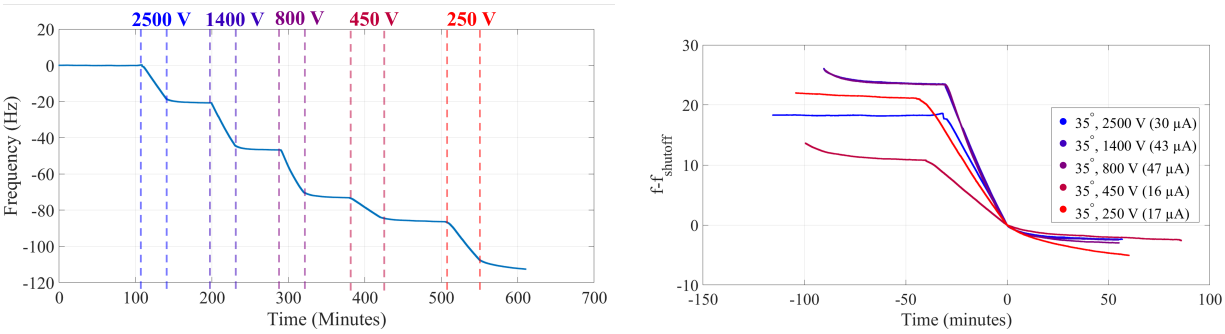

(a) Raw frequency vs time

(b) Stacked and zeroed frequency vs time

Figure 3.11: Raw measurements of QCM frequency at varying energies and a constant polar angle

As with the validation study detailed in Ch. 3.2.2, the pre- and post-deposition drift rates were calculated and compared with the frequency rate during each deposition phase. All results are tabulated in Tab. 3.3, with relative error and drift magnitude also presented.

Table 3.3: Frequency change rates and relative error for tests at varying primary energies

	Deposition	Pre-Deposition		Post-Deposition		
V_{pri} (V)	$\frac{df}{dt}$ ($\frac{\text{Hz}}{\text{min}}$)	$\frac{df}{dt}$ ($\frac{\text{Hz}}{\text{min}}$)	% Depositon	$\frac{df}{dt}$	% Deposition	% Error
250	-0.4721	-0.0130	2.7606	-0.0500	10.6001	283.9704
450	-0.2682	-0.0140	5.2143	-0.0130	4.8604	6.7862
800	-0.7727	-0.0075	0.9673	-0.0140	1.8095	87.0566
1400	-0.7665	-0.0093	1.2148	-0.0075	0.9751	19.7300
2500	-0.5827	-0.0155	2.6554	-0.0093	1.5982	39.8142

Again, the relative error in pre- and post-deposition drifts was inconsistent, but the magnitude of both drifts was determined to be low when compared to the frequency change resulting from deposition. The pre-deposition drift rate was subtracted from the deposition phase frequency rate, as plotted in Fig. 3.12a. Applying Equation (2.1) to the corrected frequency results yields the results plotted in Fig. 3.6. The normalized mass accumulation results are also presented.

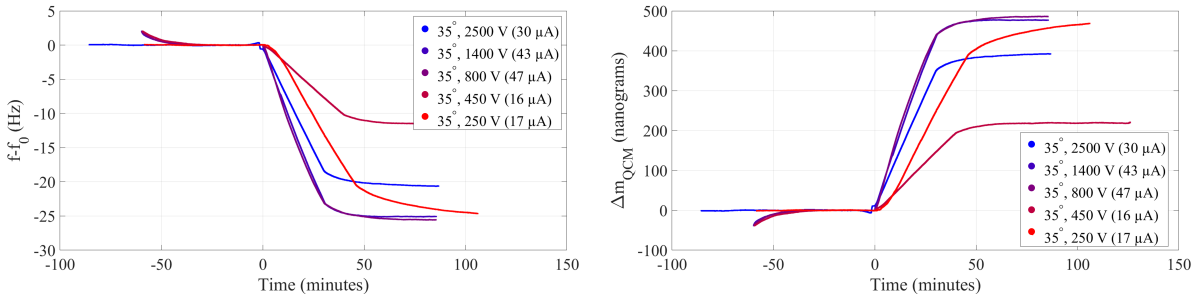

(a) Drift corrected frequency vs. time

(b) Mass deposited vs. time

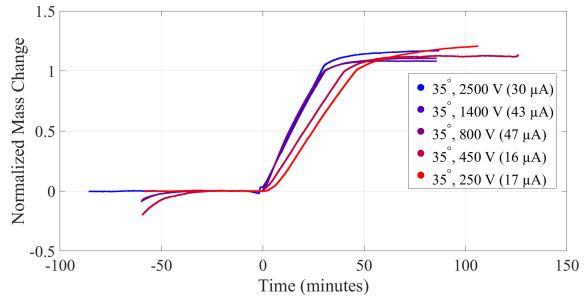

(c) Normalized mass deposition vs time

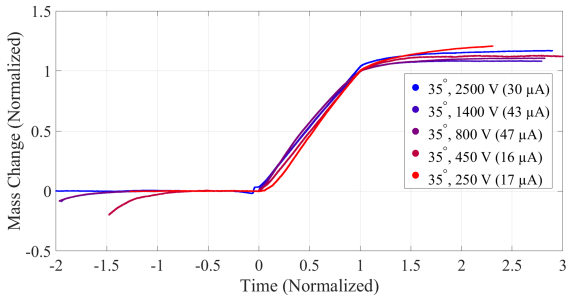

(d) Normalized mass deposition vs normalized time

Figure 3.12: Processed frequency data for varying primary energies and a constant polar angle

Yields at each time were then calculated according to Equation (3.1) and plotted in Fig. 3.13. Average yields are tabulated in Tab. 3.4.

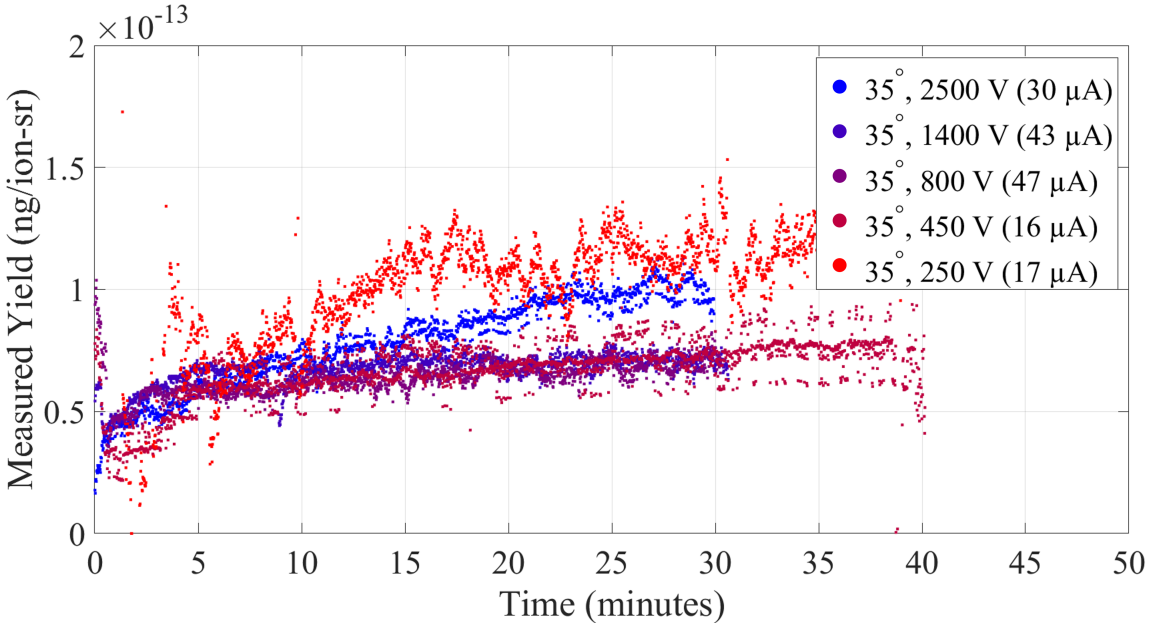

Figure 3.13: Secondary mass flux yield vs time for varying primary energies

Table 3.4: Average secondary mass flux yields at varying polar angle and constant primary energy

V_{pri} (V)	$\lvert y \rvert (\frac{\text{ng}}{\text{ion-sr}})$	$\sigma(\frac{\text{ng}}{\text{ion-sr}})$
250	8.032×10^{-14}	2.386×10^{-14}
450	7.180×10^{-14}	1.326×10^{-14}
800	6.822×10^{-14}	0.691×10^{-14}
1400	7.006×10^{-14}	0.566×10^{-14}
2500	8.873×10^{-14}	1.040×10^{-14}

These results show that the secondary mass flux yield exhibits little change across the range of primary energies, aside from slight increases at the lower and upper bounds. Further discussion and comparison of these values is presented in Ch. 4.

3.3.2 Varying Angle, Constant Primary Energy

Profiling the angular distribution of secondary mass was the goal for the next round of experiments. These tests consisted of operating the thruster at one condition across deposition events, while moving the QCM to different polar positions as shown in Ch. 2.3. Given the results described in Ch. 3.3.1, the angular profile was obtained for two different plumes: a low voltage plume produced by a thruster with a biased extractor, and a high voltage plume produced by a thruster with a grounded extractor.

Low Energy

The first angular profile was obtained with the thruster producing a low voltage primary plume. As in the tests detailed in Ch. 3.3.1, the emitter voltage was biased to ± 250 V in a 1 Hz square wave, while the extractor was biased to ∓ 1650 V in a 180° phase shifted 1 Hz square wave. The first deposition was conducted at a polar angle of 35°, and the QCM was moved by 15° between each test. Figure 3.14a shows the raw frequency measurements from the deposition tests, with Fig. 3.14b aligning the individual test measurements with $t = 0$ shifted to the thruster shutoff time in each case.

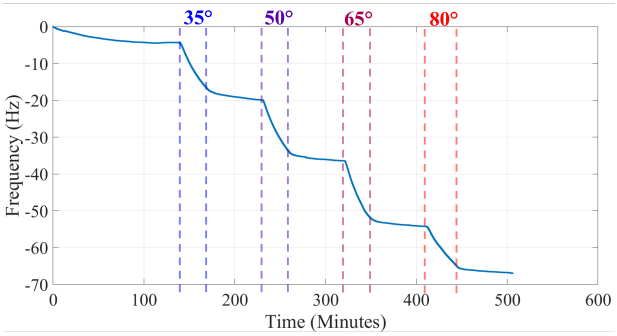

(a) Raw frequency vs time

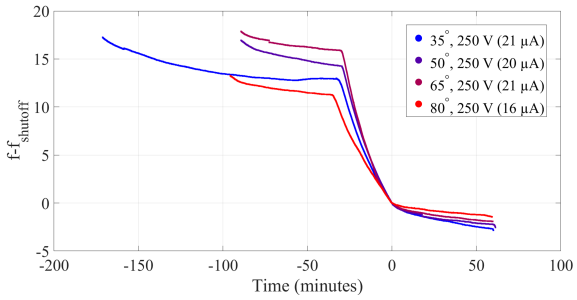

(b) Stacked and zeroed frequency vs time

Figure 3.14: Raw measurements of QCM frequency at low primary energy and varying polar angle

Frequency rates for the deposition phase as well as pre- and post-deposition settling time were calculated and tabulated in Tab. 3.5.

Table 3.5: Frequency change rates and relative error for tests conducted at low primary energy and varying polar angles

	Deposition	Pre-Deposition		Post-Deposition		
α (°)	$\frac{df}{dt}$ ($\frac{\text{Hz}}{\text{min}}$)	$\frac{df}{dt}$ ($\frac{\text{Hz}}{\text{min}}$)	% Depositon	$\frac{df}{dt}$	% Deposition	% Error
35	-0.411	-0.025	6.163	-0.030	7.202	16.846
50	-0.473	-0.030	6.260	-0.019	3.951	36.880
65	-0.526	-0.019	3.552	-0.006	1.111	68.712
80	-0.319	-0.006	1.834	-0.020	6.311	244.054

The pre-deposition drift rates were subtracted from each of the deposition phase measurements, producing the corrected frequency plot in Fig. 3.15a. The cumulative mass was then calculated and is presented in Fig. 3.15b. Normalized cumulative mass curves in Figs. 3.15c and 3.15d present an initial comparison of the deposition rates.

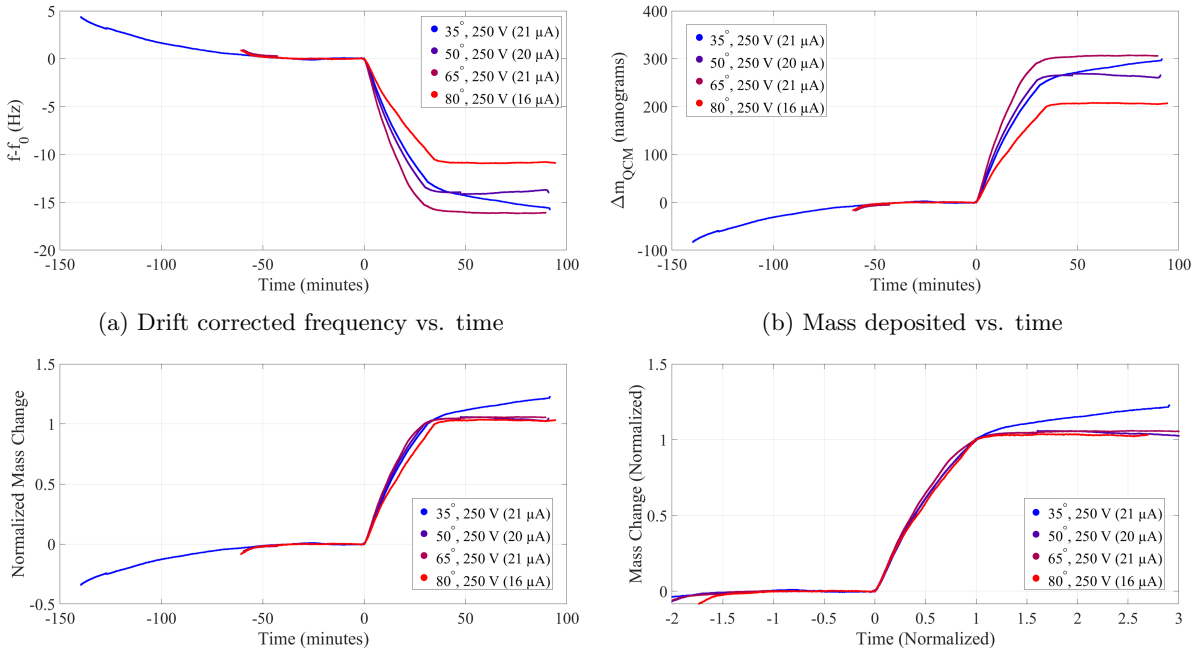

(a) Drift corrected frequency vs. time

(b) Mass deposited vs. time

(c) Normalized mass deposition vs time

(d) Normalized mass deposition vs normalized time

Figure 3.15: Processed frequency data for low primary energy and varying polar angle

The mass flux yields were then calculated at all times, and then averaged for the last 15 minutes of deposition to produce average differential mass flux yields. Figure 3.16 shows the flux yields versus time, and Tab. 3.6 displays the time averaged yields.

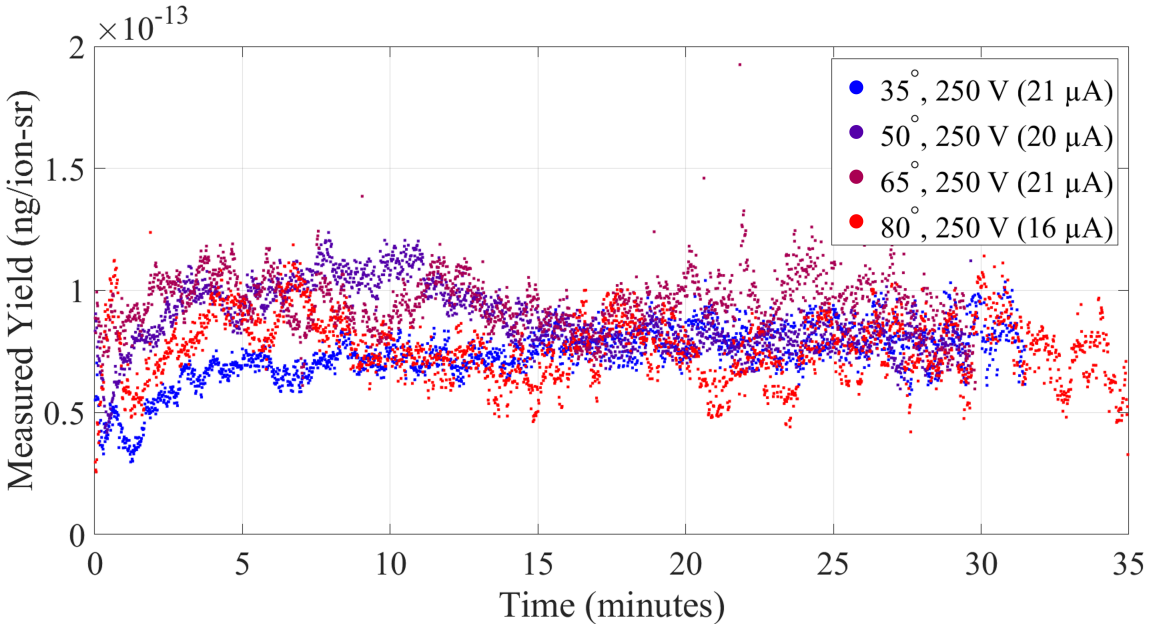

Figure 3.16: Secondary mass flux yield vs time for varying polar angles at low primary energy

Table 3.6: Average secondary mass flux yields at varying polar angle and low primary energy

α (°)	$\lvert y\rvert(\frac{\text{ng}}{\text{ion-sr}})$	$\sigma(\frac{\text{ng}}{\text{ion-sr}})$
35	8.032×10^{-14}	2.386×10^{-14}
50	8.828×10^{-14}	1.330×10^{-14}
65	8.490×10^{-14}	1.096×10^{-14}
80	7.391×10^{-14}	1.365×10^{-14}

The average mass flux yields varied only slightly across the range of polar angles, reaching a maximum at 50° and only slightly increasing as the angular position approached perpendicularity. However, all values are within a standard deviation of one another, indicating the difference cannot be entirely attributed to the change in polar angle.

High Energy

An angular profile of secondary mass flux yields from a high voltage primary plume was collected in the same procedure as described in Ch. 3.3.2. For these tests, the extractor was held at ground for all depositions, and the extractor was raised to the full extraction potential. Figure 3.17a shows the raw frequency from the full set of tests and Fig. 3.17b stacks each deposition event and sets $t = 0$ as the time when the thruster was shut off for each test.

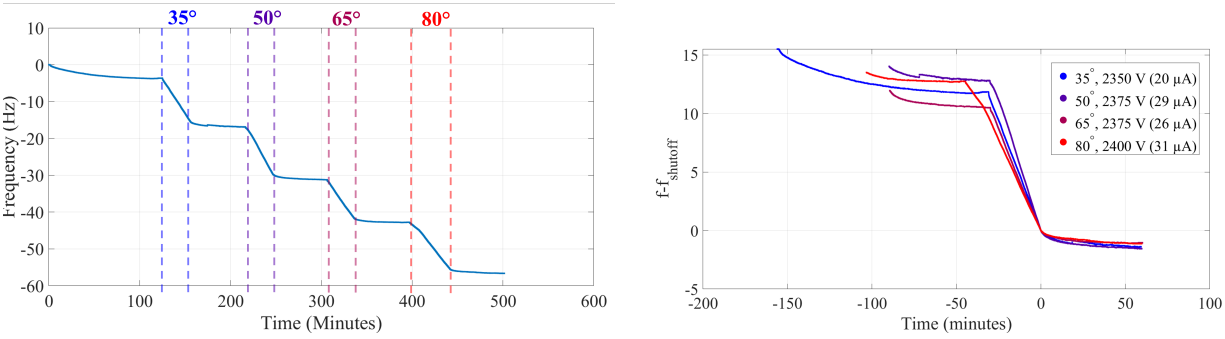

(a) Raw frequency vs time

(b) Stacked and zeroed frequency vs time

Figure 3.17: Raw measurements of QCM frequency at low primary energy and varying polar angle

The deposition and drift rates were calculated and tabulated as presented below in Tab. 3.7.

Table 3.7: Frequency change rates and relative error for tests conducted at high primary energy and varying polar angles

	Deposition	Pre-Deposition		Post-Deposition		
V_{primary} (V)	$\frac{df}{dt}$ ($\frac{\text{Hz}}{\text{min}}$)	$\frac{df}{dt}$ ($\frac{\text{Hz}}{\text{min}}$)	% Depositon	$\frac{df}{dt}$	% Deposition	% Error
35	-0.381	-0.008	1.990	-0.010	2.719	36.608
50	-0.424	-0.010	2.441	-0.008	1.978	18.969
65	-0.350	-0.008	2.394	-0.002	0.534	77.710
80	-0.285	-0.002	0.656	-0.008	2.979	353.936

Removing the effects of pre-deposition drift, Fig. 3.18a was produced, and mass deposition was calculated and plotted in Fig. 3.18b. The mass and time scale were also normalized for the sake of preliminary comparison as shown in Fig. 3.18c and Fig. 3.18d.

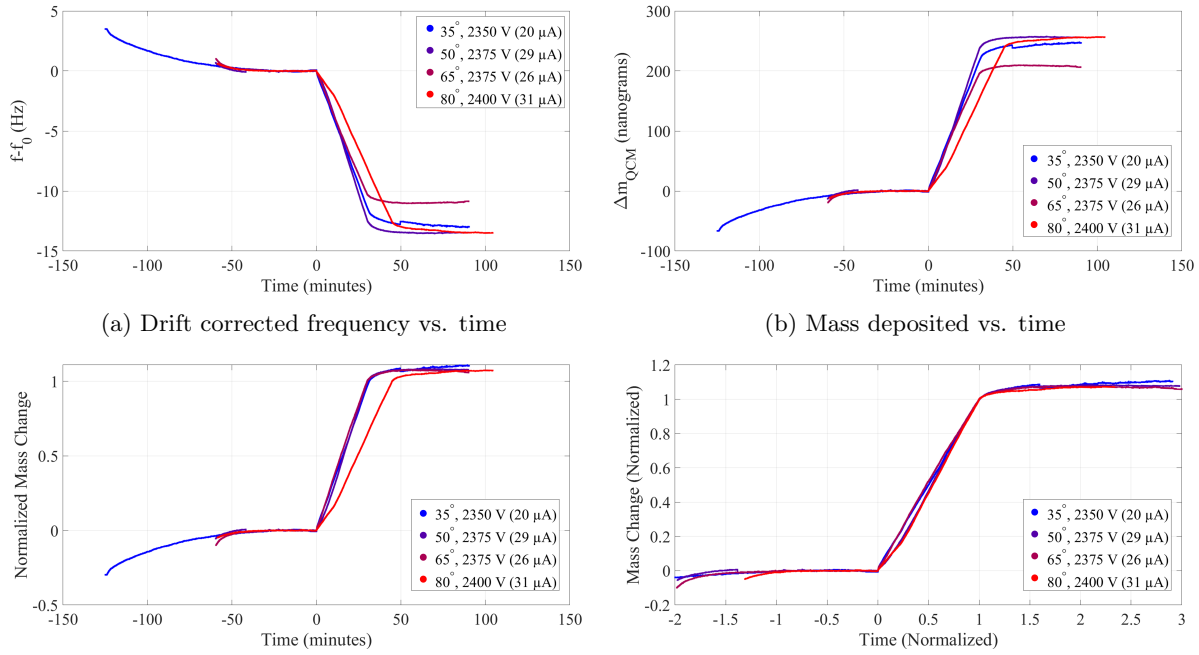

(a) Drift corrected frequency vs. time

(b) Mass deposited vs. time

(c) Normalized mass deposition vs time

(d) Normalized mass deposition vs normalized time

Figure 3.18: Processed frequency data for high primary energy and varying polar angle

The mass flux yields over time were then calculated from each test, as shown in Fig. 3.19. The average of the yields after $t = 15$ min were then calculated and tabulated in Tab. 3.8.

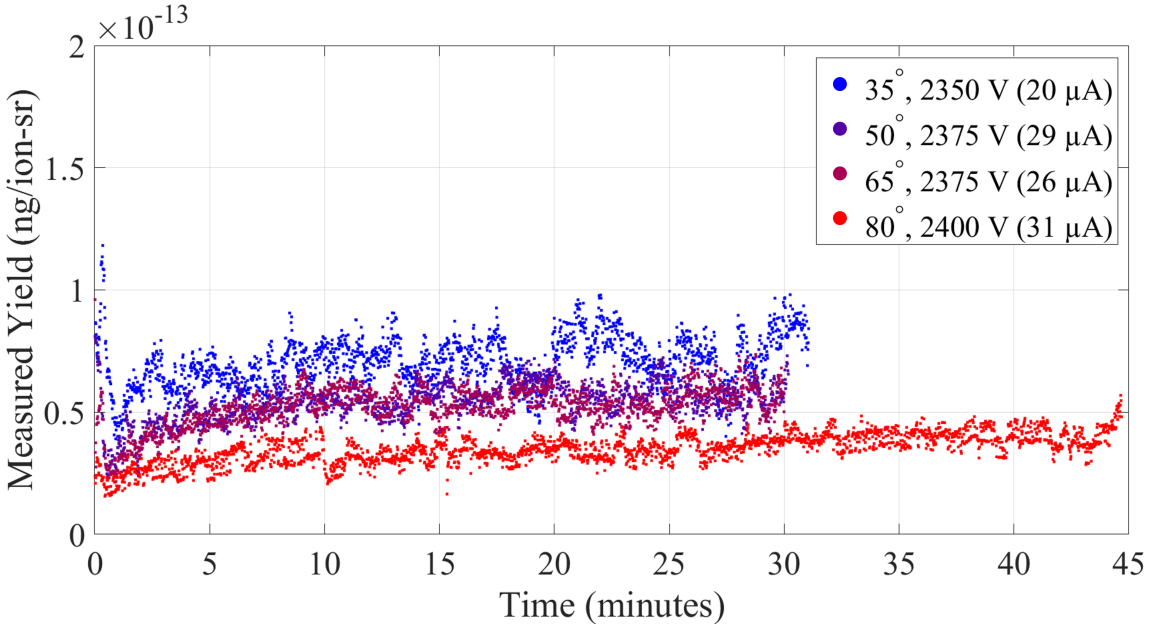

Figure 3.19: Secondary mass flux yield vs time for varying polar angles at high primary energy

Table 3.8: Average secondary mass flux yields at varying polar angle and high primary energy

α (°)	$\lvert y\rvert(\frac{\text{ng}}{\text{ion-sr}})$	$\sigma(\frac{\text{ng}}{\text{ion-sr}})$
35	7.304×10^{-14}	0.956×10^{-14}
50	5.689×10^{-14}	0.578×10^{-14}
65	5.469×10^{-14}	0.578×10^{-14}
80	3.645×10^{-14}	0.508×10^{-14}

The yields in these tests appeared to fall off as the polar angle increased. The maximum yield was measured at the smallest polar angle, with a slight decrease at 50° and 65°, and a larger dip at 80°.

Chapter 4

Discussion

4.1 Model for Secondary Plume Formation

As mentioned in Ch. 1.2, this study is amongst the first to attempt to characterize the mass of secondary plumes from electrospray plume bombardment. In addition, there are very little existing data or models for sputtering or backscattering from polyatomic ions impacting on surfaces. Therefore, a preliminary model of the production of secondary particles was devised by making a simplifying assumption about the primary collision. See Fig. 4.1 for the molecular structure of the $[EMIM]^+$ molecule.

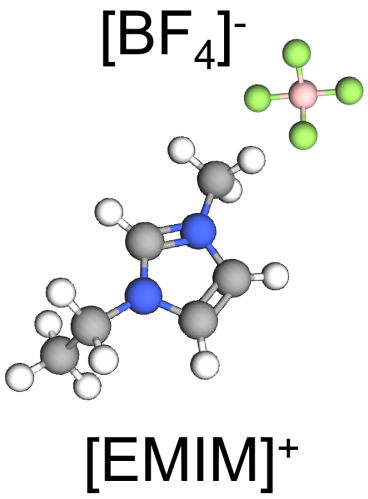

Figure 4.1: Atomic model for $[EMIM][BF_4]$

Note that the cation is largely composed of carbon atoms configured in C-C and C-H bonds. These are very weakly connected molecules, with bond energies of 6.4 and 3.5 eV, respectively. Compared to the keV

levels of energy most of the particles reach the target with, the intermolecular forces are fairly weak [33]. Further, the $[EMIM]^+$ molecule is on the order of ~10 Å across, while the spacing between nickel atoms in a polycrystalline face centered cubic structure is approximately 3.5 Å [34]; as such, penetration beyond the first atomic layer of the material is unlikely. With this context, the assumption is made that clusters and ions will interact ballistically with the nickel surface atoms and fragment into their smaller atomic components with a fraction of the molecule's initial energy. Figure 4.2 shows a sketch of potential secondary interactions using this model of primary collisions.

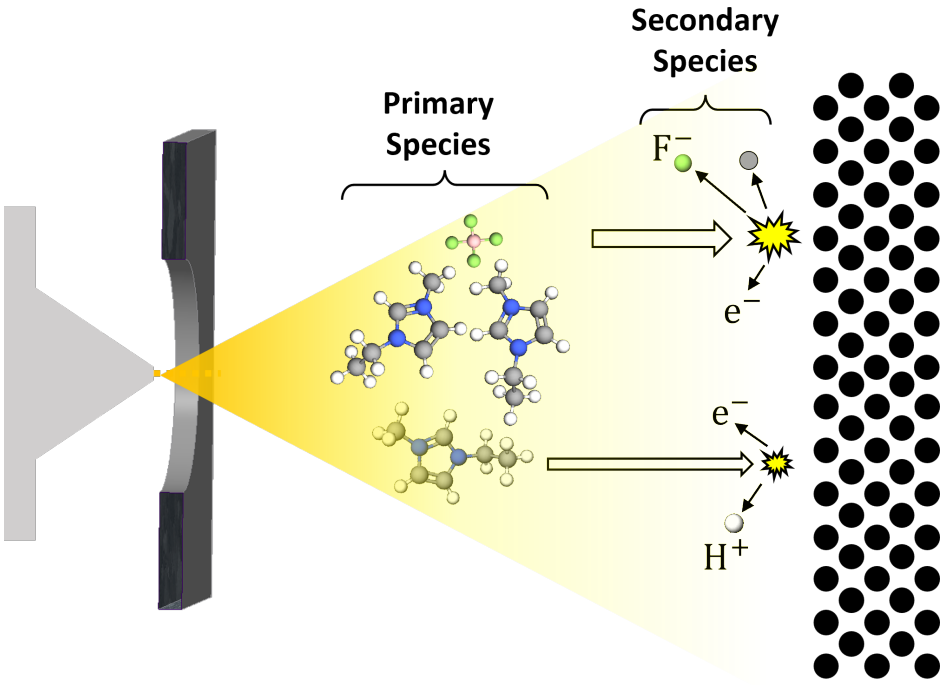

Figure 4.2: Simple model of secondary interactions as carbon-nickel collisions based on structure of $[EMIM]^+$ molecule

See below example calculations for the kinetic energy per atom at low and high primary energies.

$$m_{[EMIM]} = 111 \text{ amu}, m_C = 12 \text{ amu}$$

$$KE_{[EMIM]} = 250 \text{ eV} \Rightarrow KE_C = \frac{m_C}{m_{[EMIM]}} KE_{[EMIM]} \approx 27 \text{ eV}$$

$$KE_{[EMIM]} = 2500 \text{ eV} \Rightarrow KE_C \approx 270 \text{ eV}$$

Note that the energy per atom is well above the bond energies for alkane C-C and C-H configurations.

Applying this assumption, two methods were used to determine the expected secondary mass flux yields. Established values published by Oura et al. provide sputtering yields for carbon incident on nickel, while the software Stopping and Range of Ions in Matter (SRIM) was used to approximate of the secondary mass flux distribution for backscattering and sputtering [35]–[37].

4.2 Energy Dependence

Figure 4.3 shows the yields calculated from the tests detailed in Ch. 3.3.1 plotted against the primary plume energy in log scale.

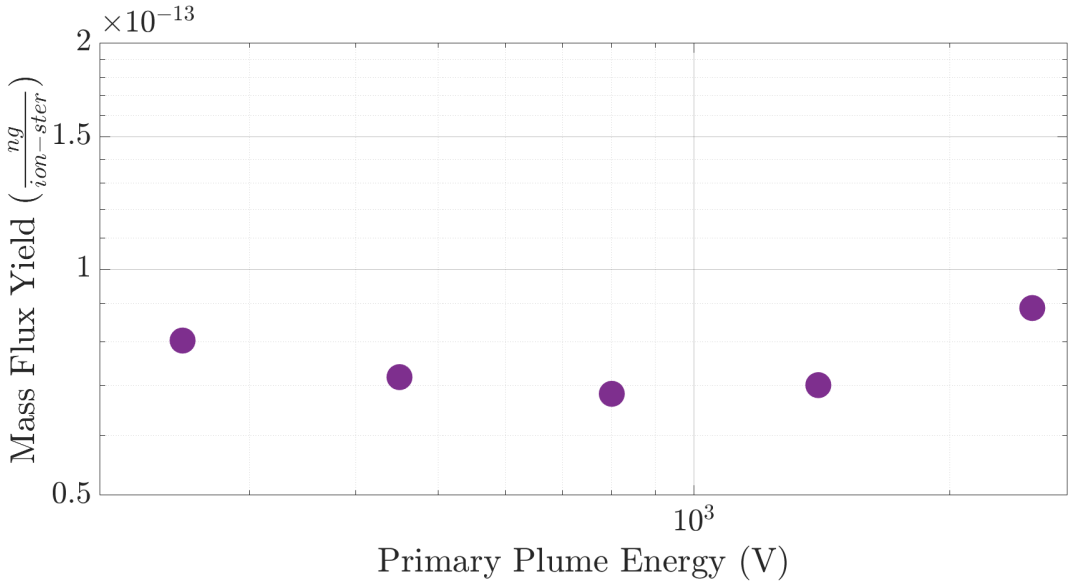

Figure 4.3: Calculated yields versus primary plume energy

Note that the yields exhibit little change across an order of magnitude of energies. This trend contradicts established values for sputtered nickel. If carbon impacts nickel at normal incidence on the range of $V_{\text{pri}} \in [27, 270]$ eV, one would expect the yields increase logarithmically as shown by Ref. [35]. Sputtering yields for most single knock-on collisions presented by Bohdansky are shown to increase as primary energy increases, with a maximum reached on the order of 10^3 eV followed by a decrease in yield at much higher energies ($> 10^4$ eV) [31], [36]. The results obtained in this study however, show little change with energy, aside from slight increases at the lowest and highest tested energies. If this small variance is attributed to the uncertainty in measurements arising from the mentioned thermal effects, then it can be presumed that the yield did not change appreciably over this range. In this case, the secondary particles resulting from ballistic collisions as detailed in Ch. 4.1 is a more plausible explanation. If the secondary particles are only a function of the geometry of the collision, then varying the energy will not have any effect. These results and

hypothesis are further considered when discussing the angular profile of the secondary mass flux.

4.3 Angular Profile

Figure 4.3 shows the angular distribution of secondary mass at both high and low primary energies. Cosine distributed sputtering and backscattering yields are also plotted for comparison. A cosine distribution is supported by both literature and first-principle calculations from SRIM [31], [37]. The lowest backscattering curve represents backscattering with 25% reflection, while the higher backscattering curve assumes 100% reflection. Sputtering and backscattering yields at normal incidence were provided from SRIM in units of atoms per ion. To match the units of $\frac{\text{ng}}{\text{ion-sr}}$, the SRIM value was divided by the 0.011 steradian solid angle formed by the QCM crystal and the center of the nickel target and multiplied by the atomic weight of nickel for the sputtering curve and the atomic weight of carbon for the backscattering curves.

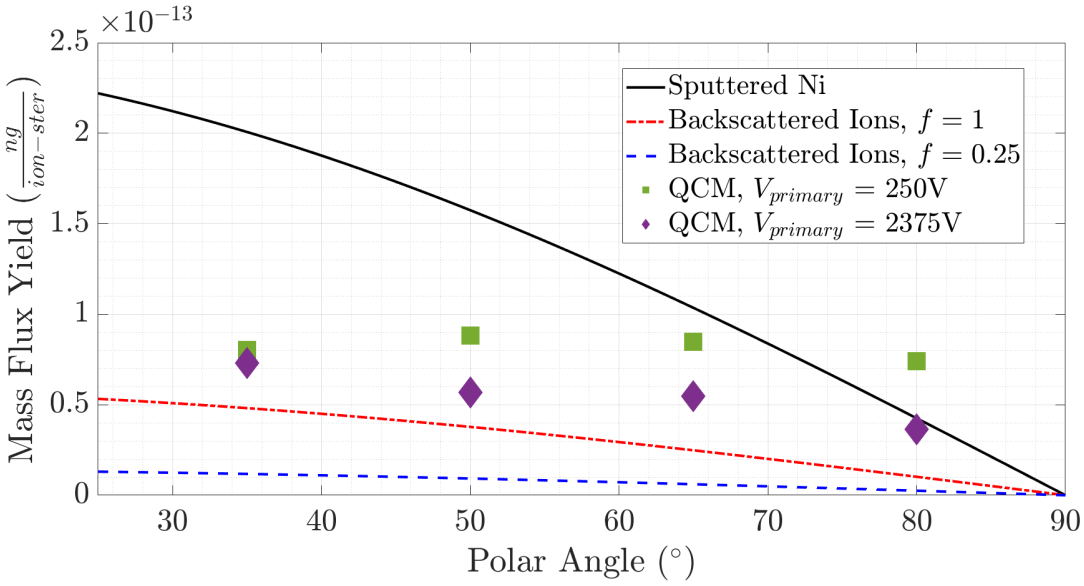

Figure 4.4: Calculated yields plotted versus polar angle with sputtering and backscattering predictions

The yields obtained from the 250 V primary plume do not trend as expected when changing the polar angle, while the yields from the high voltage plume are maximized at 35° and decrease as the polar increases. The high voltage secondary yields underestimate sputtered nickel and overestimate both 25% backscattering and total reflection. If the given model for secondary particle production holds, it can be posited that the inaccuracy of the sputtering and backscattering calculations is indicative of contributions from both phenomena when spraying a high voltage primary plume with a grounded extractor. However, the low voltage primary plume does not result in yields that reflect any of the literature or models available. This confounding result — in combination with the constant yields presented and discussed in Ch. 4.2 — indicates that the

measurements observed may be affected by an element of the experimental setup contributing significant experimental error.

4.4 Sources of Experimental Error

The measured yields from these experiments were shown to be repeatable and consistent, but the expected angular distribution of secondary mass and energy dependency of secondary flux was not observed. In order to contextualize these results and motivate future research in this area, potential sources of error in the experiments were proposed and analyzed.

4.4.1 Effects of Extractor Biasing

While the secondary mass flux yield angular distribution reflected some aspect of expected values for a high voltage primary plume, the angular profile for secondary mass from a low voltage plume appeared constant across a range of angles. Varying the energy of the primary plume also did not result in the predicted change, which could indicate a strong contribution from backscattering; however, when considering this result in concert with the aberrant angular profile from the low voltage plume, a better explanation for these results may lie in the experimental method used to produce primary electrospray plumes with a broader range of energies. As discussed in Ch. 3.1, the porous glass thruster used in these experiments only operates in a small range of emitter voltages when holding the extractor at ground. In order to produce a larger range of voltages to better represent the research interests and motivations, the operation procedure for the thruster was modified to change the extractor voltage in sync with the emitter voltage. However, no further changes were made to the thruster layout or experimental method in order to compensate for the structure of the electric field downstream of the thruster.

Much of the literature and accepted convention for electrospray thrusters and electrospray material interactions make clear that there is a "field-free" region outside of the thruster [7], [14], [38]. When not holding the extractor at ground, there is a potential differential between the extractor and the downstream target, resulting in an electric field that is relatively weak in comparison to the electric field applied to produce the plume, but not so weak as to be negligible. One likely result of this field can be demonstrated in the raw currents shown in Fig. 4.5.

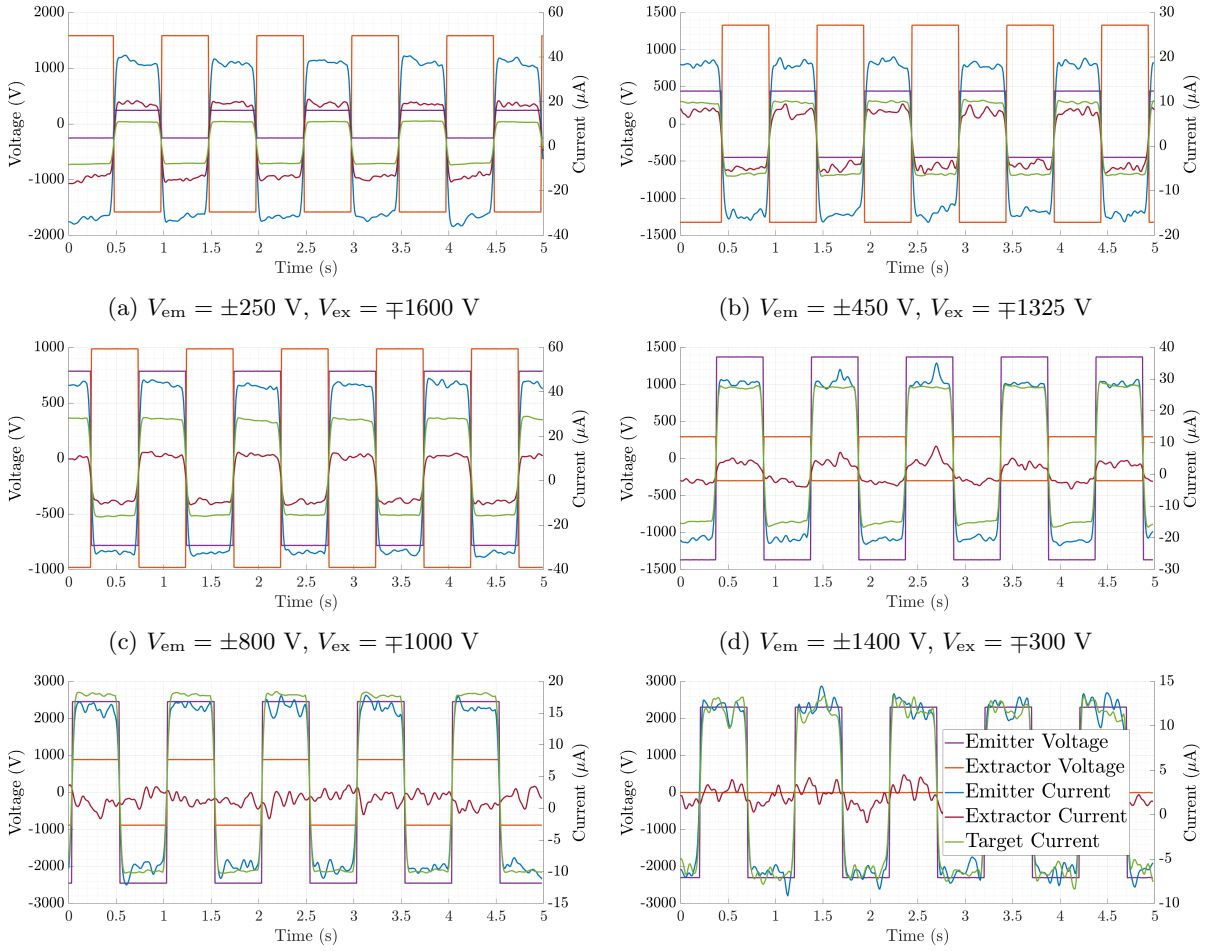

(a) $V_{em} = \pm 250$ V, $V_{ex} = \mp 1600$ V

(b) $V_{em} = \pm 450$ V, $V_{ex} = \mp 1325$ V

(c) $V_{em} = \pm 800$ V, $V_{ex} = \mp 1000$ V

(d) $V_{em} = \pm 1400$ V, $V_{ex} = \mp 300$ V

(e) $V_{em} = \pm 2500$ V, $V_{ex} = \pm 925$ V

(f) $V_{em} = \pm 2300$ V, $V_{ex} = 0$ V

Figure 4.5: Raw current traces at various emitter/extractor operation modes

Note in Fig. 4.5f that the extractor measures a fairly low current when the voltage is held at ground and the emitter voltage is raised to the full extraction potential. Figure 4.5a shows that when the extractor voltage is much higher than the emitter voltage in the opposite polarity, the extractor current is much higher. This trend persists whenever the extractor is not grounded, as shown in Figs. Figs. 4.5b to 4.5d. It is also worth noting that the extractor is electrically connected to the aluminum thruster housing, as specified in Ch. 2.1. As a result, in many of these tests, there was a large surface area of charged surface that could attract or repel charged species outside of the thruster. It is possible that due to the proximity of the thruster to the QCM in these experiments, the interactions between the charged species and the thruster exterior is impacting the secondary plume and the charged mass depositing onto the QCM. As a result, the yield values obtained in experiments with a biased extractor may be invalid, and should be limited in their consideration until improved experiments with a "cleaner" electrical environment can be conducted. One way of producing this "cleaner" environment would be to cage the thruster in a grounded shell, with an aperture to permit the

plume ions to extract unimpeded. Figure 4.6 shows a simple sketch of how the current test setup could be modified to achieve this.

4.4.2 Angular Effects

The divergent plume produced by the porous glass thruster may have also contributed to the inconsistent results. Studies on sputtering from ion beams have shown that sputtering yields and angular distributions of secondary mass tend to be strong functions of primary incidence angle [26], [27], [39]. In the experiments detailed here, the distribution of the primary plume was not controlled, and as a result, some primary ions struck the nickel target at normal incidence at the center of the target, while other ions would reach a point on the target 2 to 5 cm away from the center at a glancing angle. This lack of control over impact site and impact angle could be one reason the angular distributions detailed in Ch. 4.3 do not track well with either the cosine distributed sputtering or backscattering yields. Cosine distributions make an assumption that the plume ions impact at a single point with normal incidence. In order to better compare these results, the plume should be collimated into a unidirectional beam using an electrostatic lens. Using a device much like the one detailed in Ref. [12], a divergent electrospray plume can be collimated to a fine beam with minimal angular components without significantly changing the energetic distribution of the constituent ions. See Fig. 4.6 for an example of how this device could be implemented in the existing setup.

4.4.3 Thermal Drift

As addressed previously in Ch. 2.2, the quartz crystal microbalance used in these experiments was sensitive to changes in temperature. The background drift as observed in Fig. 3.3 is likely a result of drifting temperature while instrument electronics settle to a steady state. The results presented in Ch. 3 were collected intermittently to allow the sensor to reach a steady temperature before starting any deposition, but the thermal effects during deposition were not accounted for with any active cooling or temperature compensation. Several techniques exist to address thermal transience during deposition. Many models of QCMs include fluid lines to pass a liquid around the sensor head to carry away any heat that is transferred to the crystal while mass is being deposited [28]. By doing this, changes in sensor temperature are less pronounced, and the resultant drift is reduced. Other methods include using two crystals in a thermoelectric quartz crystal microbalance (TQCM) [25]. This setup exposes one crystal to the test environment, while keeping the second crystal isolated from the deposition process. By observing the frequency difference between the two oscillators, the effects of the deposition can be separated out from the thermal background effects. To improve upon the results obtained in these experiments, a cooled QCM — as indicated in Fig. 4.6 — should

be utilized in following investigations.

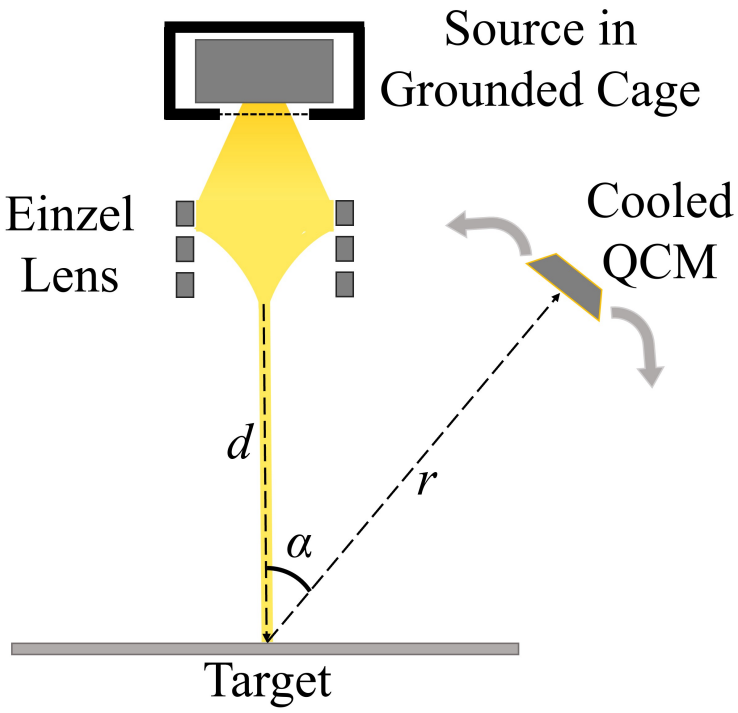

Figure 4.6: Proposed setup for modified tests to reduce sources of error

Chapter 5

Conclusions

Secondary mass flux yields from a primary electrospray plume impinging on a polycrystalline nickel surface were measured using a quartz crystal microbalance. Initial diagnostics on the porous glass thruster used to produce the plume were conducted. Mass flux yields from a high voltage primary plume dropped from 7.304×10^{-14} $\frac{\text{ng}}{\text{ion-sr}}$ at a polar angle of 35° to 3.645×10^{-14} $\frac{\text{ng}}{\text{ion-sr}}$ at 80°, with standard deviations below 1×10^{-14} $\frac{\text{ng}}{\text{ion-sr}}$. When spraying a low voltage plume, the yields were relatively constant across the set of polar angles, with values ranging from 7.391×10^{-14} $\frac{\text{ng}}{\text{ion-sr}}$ to 8.828×10^{-14} $\frac{\text{ng}}{\text{ion-sr}}$ and standard deviations as high as 2.386×10^{-14} $\frac{\text{ng}}{\text{ion-sr}}$. Analyzing the effects of primary plume energy on secondary mass flux yield, it was observed that the yields were fairly constant with high yield values of 8.032×10^{-14} $\frac{\text{ng}}{\text{ion-sr}}$ and 8.873×10^{-14} $\frac{\text{ng}}{\text{ion-sr}}$ at $V_{\text{pri}} = 250$ V and $V_{\text{pri}} = 2500$ V respectively. In between these two primary plume energies, values ranged from 6.822×10^{-14} $\frac{\text{ng}}{\text{ion-sr}}$ to 7.180×10^{-14} $\frac{\text{ng}}{\text{ion-sr}}$ with standard deviations $\leq 1.326\times10^{-14}$ $\frac{\text{ng}}{\text{ion-sr}}$. Confounding results and inconsistency with literature suggests that only the angular profile obtained with the high voltage primary plume are valid measurements of secondary mass flux, while the other datasets were influenced by an imperfect experimental setup. Regardless of this limitation, the angular profile represents a useful initial step in characterizing the plume-surface interactions for electrospray thrusters. These results can be used by experimentalists to aid in experimental design and measurement corrections. Modelers focused on electrospray systems can use this work and future improvements to better predict electrospray thruster performance and better anticipate thruster spacecraft interactions. Limitations of this study should be addressed by altering the thruster design to insulate the extractor from the thruster body, and minimizing the effects of the biased extractor by placing the thruster in a grounded cage or adding a grounded grid downstream of the extractor. Improved results could also be obtained by implementing a similar setup with a cooled QCM to minimize thermal effects. Future work on this topic should isolate the effects of positive plumes and negative plumes by

filtering the primary plume by polarity or using a thruster that can operate in a single polarity for extended amounts of time. Experiments should also characterize the effects of impact angle by collimating the plume into a equipotential beam using an Einzel or electrostatic lens.

References

[1] G. I. Taylor, "Disintegration of water drops in an electric field," *Proceedings of the Royal Society of London. Series A. Mathematical and Physical Sciences*, vol. 280, no. 1382, pp. 383–397, 1964. DOI: 10.1098/rspa.1964.0151. [Online]. Available: https://doi.org/10.1098/rspa.1964.0151.

[2] L. Rayleigh, "XX. on the equilibrium of liquid conducting masses charged with electricity," *The London, Edinburgh, and Dublin Philosophical Magazine and Journal of Science*, vol. 14, no. 87, pp. 184–186, Sep. 1882. DOI: 10.1080/14786448208628425. [Online]. Available: https://doi.org/10.1080/14786448208628425.

[3] M. M. Hohman, M. Shin, G. Rutledge, and M. P. Brenner, "Electrospinning and electrically forced jets. i. stability theory," *Physics of Fluids*, vol. 13, no. 8, pp. 2201–2220, Aug. 2001. DOI: 10.1063/1.1383791. [Online]. Available: https://doi.org/10.1063/1.1383791.

[4] A. Jaworek, "Electrospray droplet sources for thin film deposition," *Journal of Materials Science*, vol. 42, no. 1, pp. 266–297, Nov. 2006. DOI: 10.1007/s10853-006-0842-9. [Online]. Available: https://doi.org/10.1007/s10853-006-0842-9.

[5] J. B. Fenn, M. Mann, C. K. Meng, S. F. Wong, and C. M. Whitehouse, "Electrospray ionization for mass spectrometry of large biomolecules," *Science*, vol. 246, no. 4926, pp. 64–71, Oct. 1989. DOI: 10.1126/science.2675315. [Online]. Available: https://doi.org/10.1126/science.2675315.

[6] K. Clark, "Survey of electric propulsion capability," in *10th Propulsion Conference*, American Institute of Aeronautics and Astronautics, Aug. 1974. DOI: 10.2514/6.1974-1082. [Online]. Available: https://doi.org/10.2514/6.1974-1082.

[7] M. Gamero-Castano and V. Hruby, "Electrospray as a source of nanoparticles for efficient colloid thrusters," *Journal of Propulsion and Power*, vol. 17, no. 5, pp. 977–987, Sep. 2001. DOI: 10.2514/2.5858. [Online]. Available: https://doi.org/10.2514/2.5858.

[8] J. Ziemer and S. Merkowitz, "Microthrust propulsion for the LISA mission," in *40th AIAA/ASME/SAE/ASEE Joint Propulsion Conference and Exhibit*, American Institute of Aeronautics and Astronautics, Jun. 2004. DOI: 10.2514/6.2004-3439. [Online]. Available: https://doi.org/10.2514/6.2004-3439.

[9] D. G. Courtney, S. Dandavino, and H. Shea, "Comparing direct and indirect thrust measurements from passively fed ionic electrospray thrusters," *Journal of Propulsion and Power*, vol. 32, no. 2, pp. 392–407, Mar. 2016. DOI: 10.2514/1.b35836. [Online]. Available: https://doi.org/10.2514/1.b35836.

[10] J. Ziemer, "Performance of electrospray thrusters," in *31st International Electric Propulsion Conference*, American Institute of Aeronautics and Astronautics, 2009.

[11] C. Ma, "Design and characterisation of electrospray thrusters with high emission density," Ph.D. dissertation, University of Southampton, 2019.

[12] P. C. Lozano, "Studies on the ion-droplet mixed regime in colloid thrusters," Ph.D. dissertation, Massachusetts Institute of Technology, 2003, p. 222. [Online]. Available: http://ssl.mit.edu/publications/theses/PhD-2003-Lozano-TovarPaulo.pdf.

[13] M. R. Klosterman, J. L. Rovey, D. A. Levin, and A. Rao, "Ion-induced charge emission from unpolished surfaces bombarded by an [Emim][BF4] electrospray plume," *Journal of Applied Physics*, vol. 131, no. 24, 2022, ISSN: 10897550. DOI: 10.1063/5.0060615.

[14] P. Lozano and M. Martínez-Sánchez, "Ionic liquid ion sources: Characterization of externally wetted emitters," *Journal of Colloid and Interface Science*, vol. 282, no. 2, pp. 415–421, 2005, ISSN: 00219797. DOI: 10.1016/j.jcis.2004.08.132.

[15] P. Lozano and M. Martinez-Sanchez, "Efficiency estimation of EMI-BF4 ionic liquid electrospray thrusters," in *41st AIAA/ASME/SAE/ASEE Joint Propulsion Conference & Exhibit*, American Institute of Aeronautics and Astronautics, Jul. 2005. DOI: 10.2514/6.2005-4388. [Online]. Available: https://doi.org/10.2514/6.2005-4388.

[16] C. Ma and C. N. Ryan, "The Design and Characterization of a Porous-emitter Electrospray Thruster (PET-100) for Interplanetary CubeSats (CHARTS)," *Proceeding of the 7th Interplanetary CubeSat Workshop*, pp. 1–9, 2018.

[17] M. R. Natisin, H. L. Zamora, W. A. McGehee, *et al.*, "Fabrication and characterization of a fully conventionally machined, high-performance porous-media electrospray thruster," *Journal of Micromechanics and Microengineering*, vol. 30, no. 11, 2020, ISSN: 13616439. DOI: 10.1088/1361-6439/abb8c3.

[18] F. Mier-Hicks and P. Lozano, "Spacecraft-charging characteristics induced by the operation of electrospray thrusters," *Journal of Propulsion and Power*, vol. 33, no. 2, pp. 456–467, 2017. DOI: 10.2514/1.B36292.

[19] A. Thuppul, P. L. Wright, A. L. Collins, J. K. Ziemer, and R. E. Wirz, "Lifetime considerations for electrospray thrusters," *Aerospace*, vol. 7, no. 8, pp. 1–18, 2020, ISSN: 22264310. DOI: 10.3390/AEROSPACE7080108.

[20] N. M. Uchizono, A. L. Collins, C. Marrese-Reading, S. M. Arestie, J. K. Ziemer, and R. E. Wirz, "The role of secondary species emission in vacuum facility effects for electrospray thrusters," *Journal of Applied Physics*, vol. 130, no. 14, 2021, ISSN: 10897550. DOI: 10.1063/5.0063476.

[21] A. Rao, T. Bhakyapaibul, J. Rovey, D. A. Levin, and H. Chew, "Plume-material interactions of metallic surfaces bombarded by an [EMIM][BF_4] electrospray source," in *AIAA SCITECH 2023 Forum*, American Institute of Aeronautics and Astronautics, Jan. 2023. DOI: 10.2514/6.2023-1407. [Online]. Available: https://doi.org/10.2514/6.2023-1407.

[22] M. Gamero-Castaño and M. Mahadevan, "Sputtering of silicon by a beamlet of electrosprayed nanodroplets," *Applied Surface Science*, vol. 255, no. 20, pp. 8556–8561, 2009, ISSN: 01694332. DOI: 10.1016/j.apsusc.2009.06.018.

[23] D. Borodin, S. Brezinsek, J. Miettunen, *et al.*, "Determination of Be sputtering yields from spectroscopic observations at the JET ITER-like wall based on three-dimensional ERO modelling," *Physica Scripta*, vol. T159, 2014, ISSN: 02811847. DOI: 10.1088/0031-8949/2014/T159/014057.

[24] A. C. Adduci, *Characterisation of a multimode propellant operating in a porous glass electrospray thruster*, 2023.

[25] H. Cho, G.-W. Moon, S.-H. Lee, and H.-J. Seo, "Measurements of Outgassing from Satellites," in *Environmental Testing for Space Programmes*, K. Fletcher, Ed., ser. ESA Special Publication, vol. 558, Aug. 2004, pp. 445–452.

[26] J. D. Williams, M. M. Gardner, M. L. Johnson, and P. J. Wilbur, "Xenon Sputter Yield Measurements for Ion Thruster Materials," *28th International Electric Propulsion Conference*, IEPC–03–130, 2003.

[27] R. D. Kolasinski, J. E. Polk, D. Goebel, and L. K. Johnson, "Carbon sputtering yield measurements at grazing incidence," *Applied Surface Science*, vol. 254, no. 8, pp. 2506–2515, 2008, ISSN: 01694332. DOI: 10.1016/j.apsusc.2007.09.082.

[28] *Research quartz crystal microbalance instruction and operation manual*, Inficon Inc., 2014.

[29] A. Rahtu and M. Ritala, "Compensation of temperature effects in quartz crystal microbalance measurements," *Applied Physics Letters*, vol. 80, no. 3, pp. 521–523, Jan. 2002. DOI: 10.1063/1.1433904. [Online]. Available: https://doi.org/10.1063/1.1433904.

[30] A. D. Easley, T. Ma, C. I. Eneh, J. Yun, R. M. Thakur, and J. L. Lutkenhaus, "A practical guide to quartz crystal microbalance with dissipation monitoring of thin polymer films," *Journal of Polymer Science*, vol. 60, no. 7, pp. 1090–1107, Jul. 2021. DOI: 10.1002/pol.20210324. [Online]. Available: https://doi.org/10.1002/pol.20210324.

[31] J. Bohdansky, "Universal Relation for the Sputtering Yield of Monatomic Solids At Normal Ion Incidence.," *Nuclear Instruments and Methods in Physics Research, Section B: Beam Interactions with Materials and Atoms*, vol. 230 (B2), no. 1-3, pp. 587–591, 1983, ISSN: 0168583X.

[32] A. Bruno, M. Schroeder, and P. C. Lozano, "Characterization of electrospray thrusters with HAN-based monopropellants for multimode propulsion applications," in *AIAA SCITECH 2022 Forum*, American Institute of Aeronautics and Astronautics, Jan. 2022. DOI: 10.2514/6.2022-2490. [Online]. Available: https://doi.org/10.2514/6.2022-2490.

[33] J. Pitawala, J. Scheers, P. Jacobsson, and A. Matic, "Physical properties, ion–ion interactions, and conformational states of ionic liquids with alkyl-phosphonate anions," *The Journal of Physical Chemistry B*, vol. 117, no. 27, pp. 8172–8179, Jun. 2013. DOI: 10.1021/jp4042974. [Online]. Available: https://doi.org/10.1021/jp4042974.

[34] D. H. Zaitsau, K. Fumino, V. N. Emel'yanenko, A. V. Yermalayeu, R. Ludwig, and S. P. Verevkin, "Structure–property relationships in ionic liquids: A study of the anion dependence in vaporization enthalpies of imidazolium-based ionic liquids," *ChemPhysChem*, vol. 13, no. 7, pp. 1868–1876, Feb. 2012. DOI: 10.1002/cphc.201100879. [Online]. Available: https://doi.org/10.1002/cphc.201100879.

[35] K. Oura, M. Katayama, A. V. Zotov, V. G. Lifshits, and A. A. Saranin, *Surface Science: An Introduction*. Springer Berlin Heidelberg, 2003, pp. 118–119. DOI: 10.1007/978-3-662-05179-5. [Online]. Available: https://doi.org/10.1007/978-3-662-05179-5.

[36] Y. Yamamura and H. Tawara, "Energy dependence of ion-induced sputtering yields from monatomic solids at normal incidence," *Atomic Data and Nuclear Data Tables*, vol. 62, no. 2, pp. 149–253, 1996, ISSN: 0092640X. DOI: 10.1006/adnd.1996.0005.

[37] J. F. Ziegler, M. Ziegler, and J. Biersack, "SRIM – the stopping and range of ions in matter (2010)," *Nuclear Instruments and Methods in Physics Research Section B: Beam Interactions with Materials and*

Atoms, vol. 268, no. 11-12, pp. 1818–1823, Jun. 2010. DOI: 10.1016/j.nimb.2010.02.091. [Online]. Available: https://doi.org/10.1016/j.nimb.2010.02.091.

[38] R. Borrajo-Pelaez and M. Gamero-Castaño, "The effect of the molecular mass on the sputtering by electrosprayed nanodroplets," *Applied Surface Science*, vol. 344, pp. 163–170, 2015, ISSN: 01694332. DOI: 10.1016/j.apsusc.2015.03.077.

[39] R. Feder, C. Bundesmann, H. Neumann, and B. Rauschenbach, "Ion beam sputtering of Ag - Angular and energetic distributions of sputtered and scattered particles," *Nuclear Instruments and Methods in Physics Research, Section B: Beam Interactions with Materials and Atoms*, vol. 316, pp. 198–204, 2013, ISSN: 0168583X. DOI: 10.1016/j.nimb.2013.09.007. [Online]. Available: http://dx.doi.org/10.1016/j.nimb.2013.09.007.